A Variational Formulation of Dissipative Quasicontinuum Methods[☆]

O. Rokoš[a,*], L.A.A. Beex[b], J. Zeman[a], R.H.J. Peerlings[c]

[a] *Department of Mechanics, Faculty of Civil Engineering, Czech Technical University in Prague, Thákurova 7, 166 29 Prague 6, Czech Republic.*
[b] *Faculté des Sciences, de la Technologie et de la Communication, Campus Kirchberg, Université du Luxembourg 6, rue Richard Coudenhove-Kalergi, L-1359 Luxembourg.*
[c] *Department of Mechanical Engineering, Eindhoven University of Technology, P.O. Box 513, 5600 MB Eindhoven, The Netherlands.*

Abstract

Lattice systems and discrete networks with dissipative interactions are successfully employed as meso-scale models of heterogeneous solids. As the application scale generally is much larger than that of the discrete links, physically relevant simulations are computationally expensive. The QuasiContinuum (QC) method is a multiscale approach that reduces the computational cost of direct numerical simulations by fully resolving complex phenomena only in regions of interest while coarsening elsewhere. In previous work (Beex et al., *J. Mech. Phys. Solids* 64, 154–169, 2014), the originally conservative QC methodology was generalized to a virtual-power-based QC approach that includes local dissipative mechanisms. In this contribution, the virtual-power-based QC method is reformulated from a variational point of view, by employing the energy-based variational framework for rate-independent processes (Mielke and Roubíček, *Rate-Independent Systems: Theory and Application*, Springer-Verlag, 2015). By construction it is shown that the QC method with dissipative interactions can be expressed as a minimization problem of a properly built energy potential, providing solutions equivalent to those of the virtual-power-based QC formulation. The theoretical considerations are demonstrated on three simple examples. For them we verify energy consistency, quantify relative errors in energies, and discuss errors in internal variables obtained for different meshes and two summation rules.

Keywords: lattice model, quasicontinuum method, variational formulation, plasticity, multiscale modelling

[☆]The post-print version of this article published in *International Journal of Solids and Structures*, DOI: 10.1016/j.ijsolstr.2016.10.003.

[*]Corresponding author.
Email address: rokosondrej@gmail.com (O. Rokoš)

1. Introduction

Conventional continuum theories discretized by Finite Element (FE) approaches become problematic at small length-scales and complex material behaviours. In these cases, the underlying microstructure or even the atomistic crystal structure comes into play. This introduces nonlocality, and requires discrete simulations such as structural lattice computations or Molecular Statics (MS) in order to capture the physics properly. Discrete conservative systems are in their full description conveniently formulated within a variational framework, in which their behaviour follows a minimization of a potential energy $\mathcal{E}$, i.e.

$$\boldsymbol{r} = \arg\min_{\widehat{\boldsymbol{r}}\in\mathscr{R}} \mathcal{E}(\widehat{\boldsymbol{r}}), \tag{1}$$

where $\widehat{\boldsymbol{r}} \in \mathscr{R}$ denotes an arbitrary admissible vector collecting the positions of all lattice atoms (or particles), $\mathscr{R}$ denotes a configuration space, and $\boldsymbol{r} \in \mathscr{R}$ a suitable minimizer, see e.g. Tadmor and Miller (2011), Section 6. For application-scale problems, the construction of $\mathcal{E}$ and the solution of (1) entails excessive computational efforts because of two facts:

F1. A large number of atoms and bonds contained in fully-resolved systems leads to considerable expenses associated with the solution of the Euler–Lagrange equations involving large-scale energy gradients and Hessians.

F2. For the assembly of energies, gradients, and Hessians[1], all atoms or bonds have to be individually taken into account.

The QuasiContinuum (QC) methodology, originally formulated by Tadmor et al. (1996), and extended in various aspects later on, e.g. Curtin and Miller (2003); Miller and Tadmor (2002, 2009), overcomes F1 and F2 in two steps. First, *interpolation*, based on a number of selected representative atoms, or *repatoms* for short, constrains the displacements of the remaining atoms in the lattice,

$$\boldsymbol{r} = \boldsymbol{I}(\boldsymbol{r}_{\text{rep}}), \tag{2}$$

where $\boldsymbol{r}_{\text{rep}} \in \mathscr{R}_{\text{rep}}$ stores the positions of all the repatoms, and $\mathscr{R}_{\text{rep}}$ denotes a subspace of the original configuration space $\mathscr{R}$. Because the dimension of $\mathscr{R}_{\text{rep}}$ is usually much smaller than that of $\mathscr{R}$, deficiency F1 is mitigated. The second involves *summation*, in which the energy and governing equations of the reduced model are determined by collecting the contributions only from so-called *sampling atoms*, in analogy to numerical integration of FE method. As a result, an approximation $\widehat{\mathcal{E}}$ to $\mathcal{E}$ in (1) is minimized, which resolves F2. Section 3 of this paper presents a more detailed discussion of the two QC approximation steps. Other techniques and further details can be found e.g. in Tadmor and Miller (2011); Iyer and Gavini (2011); Luskin and Ortner (2013).

Also at length scales larger than the nanoscale (atomistic length scale), many materials possess discrete underlying structures—regular, irregular, or random—at the micro- or meso-scale; typical representatives are fibrous materials such as paper (Kulachenko and Uesaka,

[1] In MS, it is standard to employ quasi-Newton or completely Hessian-free minimization schemes, requiring only energies and gradients, cf. e.g. Tadmor and Miller (2011), Section 6.2. Contrary to MS, lattice systems are usually solved using a Newton-Raphson scheme that requires also Hessians.

2012; Liu et al., 2010) or textile (Potluri and Manan, 2007). In such materials the bonds between the fibres (or yarns) take the role of atoms in atomistics. However, since the involved length-scales are larger, the interactions of these "atoms" (i.e. particles) often comprise dissipative processes. Hence, the original QC formulation developed for purely conservative interactions cannot be employed. Initial theoretical developments to lift this limitation have been provided by Beex et al. (2014c,d) for fibre plasticity and bond-sliding failure. For the derivation the authors have used a non-variational thermodynamically-consistent framework that employs the following virtual-power statement

$$\dot{\widehat{\boldsymbol{r}}}^{\mathsf{T}} \boldsymbol{f}_{\text{int}} = \dot{\widehat{\boldsymbol{r}}}^{\mathsf{T}} \boldsymbol{f}_{\text{ext}}, \quad \forall \dot{\widehat{\boldsymbol{r}}}. \tag{3}$$

In Eq. (3), the dot denotes the derivative with respect to time; the vectors $\boldsymbol{f}_{\text{int}}$ and $\boldsymbol{f}_{\text{ext}}$ store components of resulting internal and external forces. This means that the left- and right-hand sides can be identified as the internal and external powers; for further details see Beex et al. (2014c), Section 2.1. Let us note that in the ideal, smooth and consistent case, the formulation of Eq. (3) would be connected to the one of (1) via the relation $\boldsymbol{f}_{\text{int}} - \boldsymbol{f}_{\text{ext}} = \partial \mathcal{E}(\widehat{\boldsymbol{r}})/\partial \widehat{\boldsymbol{r}}$. Throughout this paper, the QC approach based on Eq. (3) will be referred to as the *virtual-power-based QC*. The virtual-power-based QC framework has been employed in various contexts and proven to be efficient while accurate, see e.g. Beex et al. (2014c). However, from this formulation, it is not entirely clear whether the governing equations derived from Eq. (3) are also energetically consistent; it may happen that some terms are missing, cf. e.g. Rokoš et al. (2016), Tab. 1, for an example in continuum gradient plasticity. Variational approaches may furthermore be considered to provide finer information about system evolution such as microstructure pattern formation or phase transition, see e.g. Ortiz and Repetto (1999), Carstensen et al. (2002), and Schröder and Hackl (2013). In the case of adaptivity, better error estimates and mesh refinement capabilities for localized phenomena (such as damage) can be explored in highly nonlinear problems, cf. e.g. Radovitzky and Ortiz (1999). From a broader perspective, the variational formulation offers a consistent framework convenient for, e.g., the rigorous treatment of evolutions that exhibit discontinuities in time, investigations of structural stability using energy landscapes arising from time-incremental minimization, or direct employment of non-linear optimization algorithms. Finally, the variational formulation allows us to extend the conservative QC methodology to an entire class of rate-independent internal mechanisms in a natural way.[2]

The goal of this paper is therefore to reformulate the virtual-power-based QC framework for internal dissipative processes in terms of variational principles and show that the obtained solutions *coincide* for both formulations in the case of plasticity with isotropic hardening. To that end, a suitable potential Π will be constructed such that

$$\boldsymbol{q} \in \underset{\widehat{\boldsymbol{q}} \in \mathscr{Q}}{\arg\min}\, \Pi(\widehat{\boldsymbol{q}}), \tag{4}$$

[2]In principle, extensions to inertial and viscous effects are possible as well. For the sake of simplicity and clarity, any rate effects are omitted throughout this contribution, and the interested reader is referred to Mielke and Roubíček (2015), Chapter 5 and references therein.

describing the state of the system in analogy to (1). Here, however, $\boldsymbol{q}$ denotes a general state variable that also includes internal dissipative variables. Furthermore, $\mathscr{Q}$ is an abstract state space, and the inclusion sign $\in$ indicates that the potential Π is generally nonsmooth or may have multiple minima. In analogy to standard QC, a reduced variable $\boldsymbol{q}_{\text{red}} \in \mathscr{Q}_{\text{red}}$ and an approximate energy $\widehat{\Pi}$ will be introduced in order to alleviate F1 and F2. In what follows, the approach based on Eq. (4) will be referred to as the *variational QC*. Its construction falsifies the statement presented in Beex et al. (2014c), Section 1, claiming that the solution to Eq. (3) *cannot* be obtained by direct minimization of an energy potential.

In order to construct the full energy potential Π, we employ the variational formulation of rate-independent processes as introduced in an *abstract setting* by Mielke and Roubíček (2015) that is closely related to applications in continuum mechanics. Earlier studies were provided e.g. by Francfort and Marigo (1993), Han and Reddy (1995), Francfort and Marigo (1998), Ortiz and Stainier (1999), Charlotte et al. (2000), Hackl and Fischer (2008), Conti and Ortiz (2008), and Kochmann and Hackl (2010). Section 2 of this paper first briefly introduces definitions and basic principles of the theory. Second, the approach is reformulated in the particular context of discrete lattice systems.

The governing equations associated with (4) will be addressed in Section 4, where we recall the Alternating Minimization (AM) method, see also Bourdin et al. (2000). Since the energy potential Π for plasticity is nonsmooth, we will also briefly discuss the return-mapping algorithm suitable for its minimization.

Before closing this contribution by a summary and conclusions in Section 6, we perform numerical tests on three benchmark examples presented in Section 5, two of which have been adopted from Beex et al. (2014c), Section 4, and Beex et al. (2015b), Section 4.2. We demonstrate that both approaches, represented by Eqs. (3) and (4), lead to energetically-consistent solutions for the exact and central summation rules presented in Beex et al. (2011) and Beex et al. (2014b). The third example then presents both global as well as local quantities for an indentation test. Finally, we show that despite the significant dimension reduction and time savings achieved by the QC method, the obtained errors in stored and dissipated energies due to interpolation and summation are rather low: the relative errors in energies do not exceed 4 %, while the simulation time is decreased by a factor of $4 - 30$ depending on the triangulation, loading, and geometry.

2. Rate-Independent Variational Plasticity

2.1. General Considerations

The variational formulation for rate-independent processes comprises several steps and relies on two principles (S) and (E), which are described below (for details see Mielke, 2002; Mielke and Theil, 2004; Mielke, 2004; Mielke and Roubíček, 2015). The state of the system within a fixed time horizon $[0, T]$ is described in terms of a non-dissipative variable $\boldsymbol{r}(t) \in \mathscr{R}$, and a dissipative component $\boldsymbol{z}(t) \in \mathscr{Z}$. The latter specifies all irreversible processes at time $t \in [0, T]$, where t denotes a pseudo-time parametrizing the quasi-static evolution process. The state of the system is fully characterized by the state variable $\boldsymbol{q}(t) = (\boldsymbol{r}(t), \boldsymbol{z}(t)) \in \mathscr{Q} = \mathscr{R} \times \mathscr{Z}$. Furthermore, we consider the total free (Helmholtz type)

energy of the system $\mathcal{E} : [0,T] \times \mathscr{Q} \to \mathbb{R}$ together with the dissipation distance $\mathcal{D}(\boldsymbol{z}_2, \boldsymbol{z}_1)$, $\mathcal{D} : \mathscr{Z} \times \mathscr{Z} \to \mathbb{R}^+ \cup \{+\infty\}$ which specifies the minimum amount of energy spent by the continuous transition between two consecutive states $\boldsymbol{z}_1$ and $\boldsymbol{z}_2$; a rigorous definition and further details on $\mathcal{D}$ can be found in Mielke and Roubíček (2015), Section 3.2. Then, the process $\boldsymbol{q} : [0,T] \to \mathscr{Q}$ is called an energetic solution to the initial-value problem described by $(\mathcal{E}, \mathcal{D}, \boldsymbol{q}_0)$ if it satisfies the following two principles (S) and (E), together with an initial condition (I):

(S) **Global stability:** for all $t \in [0,T]$ and for all $\widehat{\boldsymbol{q}} \in \mathscr{Q}$

$$\mathcal{E}(t, \boldsymbol{q}(t)) \leq \mathcal{E}(t, \widehat{\boldsymbol{q}}) + \mathcal{D}(\widehat{\boldsymbol{z}}, \boldsymbol{z}(t)), \tag{S}$$

which requires the solution to be the global minimum of the sum $\mathcal{E} + \mathcal{D}$. To see this recall that the definition of the global minimum of $\mathcal{E} + \mathcal{D}$ reads

$$\mathcal{E}(t, \boldsymbol{q}(t)) + \mathcal{D}(\boldsymbol{z}(t), \boldsymbol{z}(s)) \leq \mathcal{E}(t, \widehat{\boldsymbol{q}}) + \mathcal{D}(\widehat{\boldsymbol{z}}, \boldsymbol{z}(s)), \tag{5}$$

where $\boldsymbol{q}(s) \in \mathscr{Q}$ denotes previous configuration at time $s \leq t$. As $\mathcal{D}$ is an extended-quasidistance function (for definition see e.g. Mielke and Roubíček 2015, Section 2.1.1), it satisfies the triangle inequality $\mathcal{D}(\widehat{\boldsymbol{z}}, \boldsymbol{z}(s)) \leq \mathcal{D}(\boldsymbol{z}(t), \boldsymbol{z}(s)) + \mathcal{D}(\widehat{\boldsymbol{z}}, \boldsymbol{z}(t))$, which used in (5) provides (S).

(E) **Energy equality:** for all $t \in [0,T]$

$$\mathcal{E}(t, \boldsymbol{q}(t)) + \mathrm{Var}_{\mathcal{D}}(\boldsymbol{q}; 0, t) = \mathcal{E}(0, \boldsymbol{q}(0)) + \int_0^t \mathcal{P}(s)\,\mathrm{d}s, \tag{E}$$

which expresses the energy balance in terms of the internal energy, the dissipated energy $\mathrm{Var}_{\mathcal{D}}$, and the time-integrated power of external forces $\mathcal{P}$.

(I) **Initial condition:**

$$\boldsymbol{q}(0) = \boldsymbol{q}_0. \tag{I}$$

In the second principle (E), the dissipation along a curve $\boldsymbol{q}$ is expressed as

$$\mathrm{Var}_{\mathcal{D}}(\boldsymbol{q}; 0, t) = \sup\left\{\sum_{k=1}^{n} \mathcal{D}(\boldsymbol{z}(t_k), \boldsymbol{z}(t_{k-1}))\right\}, \tag{6}$$

where the supremum is taken over all $n \in \mathbb{N}$ and all partitions of the time interval $[0,t]$, $0 = t_0 < t_1 < \cdots < t_n = t$. Introducing a time discretization of $[0,T]$, the two principles (S) and (E) along with initial condition (I) naturally give rise to an

(IP) **Incremental problem:** for $k = 1, \ldots, n_T$

$$\boldsymbol{q}(t_k) \in \operatorname*{arg\,min}_{\widehat{\boldsymbol{q}} \in \mathscr{Q}} \Pi^k(\widehat{\boldsymbol{q}}; \boldsymbol{q}(t_{k-1})) \tag{IP}$$

amenable to a numerical solution in which each step is realized as a minimization problem of an incremental energy

$$\Pi^k(\widehat{\boldsymbol{q}}; \boldsymbol{q}(t_{k-1})) = \mathcal{E}(t_k, \widehat{\boldsymbol{q}}) + \mathcal{D}(\widehat{\boldsymbol{z}}, \boldsymbol{z}(t_{k-1})). \tag{7}$$

The main conceptual difficulty with (IP) is that it represents a global minimization problem, which is computationally cumbersome for non-convex energies. It is reasonable, however, to assume that stable solutions of (IP) are associated with local minima. Then, multiple minimizers can exist, but only the ones satisfying (E) are adopted as proper solutions. It has been shown that as long as the solution $\boldsymbol{q}(t)$ remains continuous in time, the energy balance holds (see Pham et al. 2011; Pham and Marigo 2013). In the examples in Section 5 we verify that this is indeed the case for hardening plasticity, thereby justifying the local minimization approach adopted in this work. As a result, the energy balance (E) need not be enforced explicitly.

2.2. Lattices with Dissipative Internal Processes

To specify the above formulation for lattice systems, we start by introducing a geometrical setting and necessary notation (depicted in Fig. 1), followed by explicit definitions of energies. Before doing so, let us mention that the term "atoms" is meant to represent individual particles or nodes of the underlying (non-atomistic) lattice, consistently with the original QC methodology developed for atomistic systems. Furthermore, for clarity we confine our exposition to two spatial dimensions; the extension to three dimensions is straightforward.

2.2.1. Geometry and Internal Variables

The domain $\Omega_0 \subset \mathbb{R}^2$ in a reference configuration contains a set N_{ato} of $n_{\text{ato}} = \#N_{\text{ato}}$ atoms, where $\#\bullet$ returns the cardinality of a set $\bullet$. The reference spatial position of each atom $\alpha \in N_{\text{ato}}$ is specified by a vector $\boldsymbol{r}_0^\alpha \in \mathbb{R}^2$, and can be expressed as a linear combination of primitive vectors in analogy to the Bravais lattices since we confine our attention to regular structures only.[3] All positions $\boldsymbol{r}_0^\alpha$ are collected in a column matrix $\boldsymbol{r}_0 = [\boldsymbol{r}_0^1, \dots, \boldsymbol{r}_0^{n_{\text{ato}}}]^\mathsf{T}$, $\boldsymbol{r}_0 \in \mathbb{R}^{2\,n_{\text{ato}}}$, for convenience. Note that throughout this paper, Greek indices refer to atom numbers whereas Latin indices are reserved for spatial coordinates or other integer parametrizations. Each atom α is further attributed with a set $B_\alpha \subset N_{\text{ato}}$ of its nearest neighbours; recall that for the truss structures of interest, the Verlet list—i.e. the lists of all the neighbours B_α for all atoms $\alpha \in N_{\text{ato}}$—does not change in time. The distance between two atoms α and β and the list of all inter-atomic distances in the reference configuration are denoted as

$$r_0^{\alpha\beta}(\boldsymbol{r}_0) = ||\boldsymbol{r}_0^\beta - \boldsymbol{r}_0^\alpha||_2, \tag{8a}$$

$$\{r_0^{\alpha\beta}(\boldsymbol{r}_0)\} = \{r_0^{\alpha\beta} \,|\, \alpha = 1, \dots, n_{\text{ato}},\ \beta \in B_\alpha,\ \text{duplicity removed}\}, \tag{8b}$$

[3] For the sake of clarity, we consider only nearest-neighbour interactions in what follows, although the presented theory can be easily generalized to long-range or multi-body interactions. For extensions to beam structures see e.g. Beex et al. (2014a).

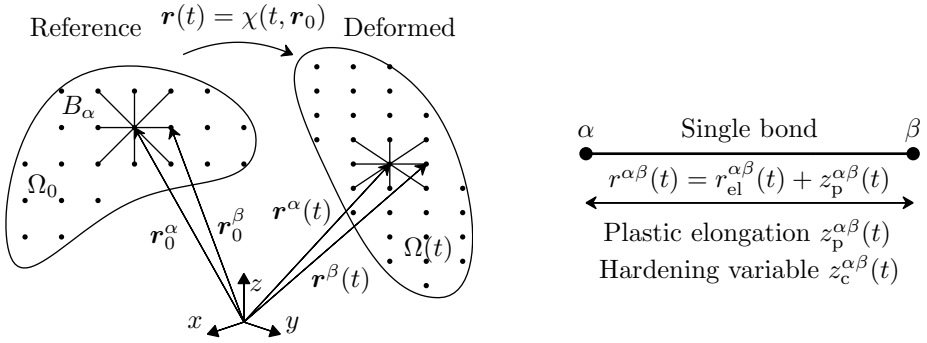

(a) configurations and kinematics (b) single bond

Figure 1: Sketch of (a) geometric variables and two system configurations, reference Ω_0 and current $\Omega(t)$, and (b) single bond setup.

where $||\bullet||_2$ represents the Euclidean norm. Since $r_0^{\alpha\beta} = r_0^{\beta\alpha}$, the set $\{r_0^{\alpha\beta}\}$ in (8b) consists of n_{bon} components, where n_{bon} is the number of all the bonds of the system collected in a set N_{bon}, i.e. $\#N_{\mathrm{bon}} = n_{\mathrm{bon}}$. Throughout this paper we employ the symbol $\alpha\beta$ in two contexts: in the context of atoms, $r_0^{\alpha\beta}$ means the distance in the reference configuration between two atoms $\alpha, \beta \in N_{\mathrm{ato}}$ (as used above), whereas in the context of bonds the same symbol $r_0^{\alpha\beta}$ means the length of the p-th bond in the reference configuration, $p = \alpha\beta$, $p \in N_{\mathrm{bon}}$, with end atoms $\alpha, \beta \in N_{\mathrm{ato}}$; a similar convention applies to other physical quantities.

Deformation mapping $\chi(t, \boldsymbol{r}_0)$ transforms Ω_0 from the reference to the current configuration $\Omega(t) \subset \mathbb{R}^2$, where the locations of the atoms are specified by position vectors $\boldsymbol{r}^\alpha(t)$, $\alpha = 1, \ldots, n_{\mathrm{ato}}$. In analogy to $\boldsymbol{r}_0$, we collect all $\boldsymbol{r}^\alpha$ in a column matrix $\boldsymbol{r}(t) = [\boldsymbol{r}^1(t), \ldots, \boldsymbol{r}^{n_{\mathrm{ato}}}(t)]^{\mathsf{T}}$, $\boldsymbol{r}(t) \in \mathbb{R}^{2\,n_{\mathrm{ato}}}$, that represents also the abstract non-dissipative variable[4]. Furthermore, we introduce the distance measure between two atoms $r^{\alpha\beta}(\boldsymbol{r}(t))$, and the set of all distances $\{r^{\alpha\beta}(\boldsymbol{r}(t))\}$, cf. Eq. (8). Due to the time-dependent Dirichlet boundary conditions and possible kinematic constraints, $\mathscr{R}(t)$ is a function of time and it forms a manifold in $\mathbb{R}^{2\,n_{\mathrm{ato}}}$.

Each bond is further endowed with two internal variables: the plastic slip or elongation of the bond $z_{\mathrm{p}}^{\alpha\beta}(t)$, and the cumulative plastic slip (a hardening variable) $z_{\mathrm{c}}^{\alpha\beta}(t)$. For clarity, we introduce column matrices $\boldsymbol{z}_{\mathrm{p}}(t)$ and $\boldsymbol{z}_{\mathrm{c}}(t)$, both in $\mathbb{R}^{n_{\mathrm{bon}}}$, collecting $z_{\mathrm{p}}^{\alpha\beta}(t)$ and $z_{\mathrm{c}}^{\alpha\beta}(t)$ of all bonds. Then, the abstract dissipative variable can be specified as $\boldsymbol{z}(t) = (\boldsymbol{z}_{\mathrm{p}}(t), \boldsymbol{z}_{\mathrm{c}}(t))$, and $\mathscr{Z}$ as $\mathbb{R}^{2\,n_{\mathrm{bon}}}$ (recall that $\boldsymbol{z}(t) \in \mathscr{Z}$).

2.2.2. Definition of Energies

Having described the physical variables, we proceed to the formal definitions of the energies. Because no external forces will be used, the elastic part of the incremental energy

[4]Strictly speaking, the non-dissipative component should consist of $\boldsymbol{r}_{\mathrm{el}}^{\alpha\beta}$ for appropriate α and β, where $\boldsymbol{r}_{\mathrm{el}}^{\alpha\beta} = \boldsymbol{r}^{\alpha\beta} - \frac{\boldsymbol{r}^{\alpha\beta}}{r^{\alpha\beta}} z_{\mathrm{p}}^{\alpha\beta}$. Because such an affine transformation does not affect the results, we adopt $\boldsymbol{r}^{\alpha\beta}$ instead of $\boldsymbol{r}_{\mathrm{el}}^{\alpha\beta}$ as our primal variables from now on for convenience.

is not an explicit function of time t and reads as

$$\mathcal{E}(\widehat{\boldsymbol{q}}) = \mathcal{V}_{\text{int}}(\widehat{\boldsymbol{r}}, \widehat{\boldsymbol{z}}_{\text{p}}) + \mathcal{V}_{\text{hard}}(\widehat{\boldsymbol{z}}_{\text{c}}). \tag{9}$$

Note that hatted variables $\widehat{\bullet}$ represent an arbitrary admissible configuration of the system, whereas the absence of hats indicates that these state variables are minimizers of (IP), see also Eq. (7). The interatomic potential energy $\mathcal{V}_{\text{int}}$ in (9) specifies a recoverable part of the energy stored in all atom interactions. It is sufficient to adhere to pair potentials, for which

$$\mathcal{V}_{\text{int}}(\widehat{\boldsymbol{r}}, \widehat{\boldsymbol{z}}_{\text{p}}) = \mathcal{V}_{\text{int}}(\{\widehat{r}^{\alpha\beta}(\boldsymbol{r})\}, \widehat{\boldsymbol{z}}_{\text{p}}) = \frac{1}{2} \sum_{\alpha,\beta \in B_\alpha} \phi^{\alpha\beta}(\widehat{r}^{\alpha\beta}, \widehat{z}_{\text{p}}^{\alpha\beta}), \tag{10}$$

where the first equality holds as a consequence of the principle of potential invariance. Note that permutation symmetry requires $\phi^{\alpha\beta} = \phi^{\beta\alpha}$, and that $\phi^{\alpha\beta}$ corresponds to the elastic portion of the energy stored in a single bond stretched to a length $\widehat{r}^{\alpha\beta}$ with a plastic elongation $\widehat{z}_{\text{p}}^{\alpha\beta}$. Further,

$$\mathcal{V}_{\text{hard}}(\widehat{\boldsymbol{z}}_{\text{c}}) = \frac{1}{2} \sum_{\alpha,\beta \in B_\alpha} h^{\alpha\beta}(\widehat{z}_{\text{c}}^{\alpha\beta}) \tag{11}$$

reflects an unrecoverable part of the stored energy, locked in all bonds due to hardening effects, where $h^{\alpha\beta}(\bullet)$ denotes the hardening pair potential of a single bond. The dissipation distance for a single bond, $\mathcal{D}^{\alpha\beta}$, between two different states $\widehat{\boldsymbol{z}}_1$ and $\widehat{\boldsymbol{z}}_2$ is defined as

$$\mathcal{D}^{\alpha\beta}(\widehat{\boldsymbol{z}}_2, \widehat{\boldsymbol{z}}_1) = \begin{cases} f_0^{\alpha\beta} |\widehat{z}_{\text{p},2}^{\alpha\beta} - \widehat{z}_{\text{p},1}^{\alpha\beta}| & \text{if } \widehat{z}_{\text{c},2}^{\alpha\beta} \geq \widehat{z}_{\text{c},1}^{\alpha\beta} + |\widehat{z}_{\text{p},2}^{\alpha\beta} - \widehat{z}_{\text{p},1}^{\alpha\beta}| \\ +\infty & \text{otherwise,} \end{cases} \quad \alpha\beta = 1, \dots, n_{\text{bon}}, \tag{12}$$

where $f_0^{\alpha\beta} > 0$ is an initial yield force. The total dissipation distance then collects the contributions of all bonds, namely

$$\mathcal{D}(\widehat{\boldsymbol{z}}_2, \widehat{\boldsymbol{z}}_1) = \frac{1}{2} \sum_{\alpha,\beta \in B_\alpha} \mathcal{D}^{\alpha\beta}(\widehat{\boldsymbol{z}}_2, \widehat{\boldsymbol{z}}_1). \tag{13}$$

Note that setting $\mathcal{V}_{\text{hard}} = \mathcal{D} = 0$ and $\boldsymbol{z}(t) = \boldsymbol{0}$ reduces (IP) to standard MS defined in Eq. (1); for further details we refer the interested reader to, e.g., Tadmor and Miller (2011), Chapter 6.

Let us close this section with the observation that the total incremental energy Π^k can be expressed in two equivalent forms: as a sum over all atom sites such as described above, or as a sum over all bonds. This allows us, therefore, to introduce the incremental bond, $\widetilde{\pi}_{\alpha\beta}^k$, and site, $\widehat{\pi}_\alpha^k$, energies of the form

$$\widetilde{\pi}_{\alpha\beta}^k(\widehat{\boldsymbol{q}}; \boldsymbol{q}(t_{k-1})) = \phi^{\alpha\beta}(\widehat{r}^{\alpha\beta}, \widehat{z}_{\text{p}}^{\alpha\beta}) + h^{\alpha\beta}(\widehat{z}_{\text{c}}^{\alpha\beta}) + \mathcal{D}^{\alpha\beta}(\widehat{\boldsymbol{z}}, \boldsymbol{z}(t_{k-1})), \ \alpha\beta = 1, \dots, n_{\text{bon}}, \tag{14a}$$

$$\widehat{\pi}_\alpha^k(\widehat{\boldsymbol{q}}; \boldsymbol{q}(t_{k-1})) = \frac{1}{2} \sum_{\beta \in B_\alpha} \widetilde{\pi}_{\alpha\beta}^k(\widehat{\boldsymbol{q}}, \boldsymbol{q}(t_{k-1})), \ \alpha = 1, \dots, n_{\text{ato}}, \tag{14b}$$

and write

$$\Pi^k(\widehat{\boldsymbol{q}};\boldsymbol{q}(t_{k-1})) = \sum_{\alpha\beta=1}^{n_{\mathrm{bon}}} \widetilde{\pi}^k_{\alpha\beta}(\widehat{\boldsymbol{q}};\boldsymbol{q}(t_{k-1})) = \sum_{\alpha=1}^{n_{\mathrm{ato}}} \widehat{\pi}^k_{\alpha}(\widehat{\boldsymbol{q}};\boldsymbol{q}(t_{k-1})). \tag{15}$$

The reason for introducing two equivalent expressions for Π^k is that the site energies (14b) are convenient for the minimization of (IP) with respect to the kinematic variable $\widehat{\boldsymbol{r}}$, whereas the bond energies (14a) are more suitable for the minimization with respect to the internal variable $\widehat{\boldsymbol{z}}$.

3. Quasicontinuum Methodology

Let us proceed to the two QC steps introduced to mitigate excessive computational demands implied by F1 and F2 that are inherently associated with the minimization problems (1) and (IP) for conservative and dissipative systems. In the two sections below, on interpolation and summation, we explain how these steps apply on the incremental energy Π^k.

3.1. Interpolation

Upon specifying a subset of atoms $N^{\mathrm{ato}}_{\mathrm{rep}} \subseteq N_{\mathrm{ato}}$, $\#N^{\mathrm{ato}}_{\mathrm{rep}} = n_{\mathrm{rep}} \ll n_{\mathrm{ato}}$ that determine the deformation state of the system, one can reconstruct the positions of all the remaining atoms through interpolation:

$$\widehat{\boldsymbol{r}} = \boldsymbol{\Phi}\widehat{\boldsymbol{r}}_{\mathrm{rep}}, \tag{16}$$

cf. Eq. (2). Here, $\widehat{\boldsymbol{r}}_{\mathrm{rep}} \in \mathscr{R}_{\mathrm{rep}}(t)$ represents a column matrix of all representative atoms' position vectors for any admissible configuration, and the matrix $\boldsymbol{\Phi}$ stores the basis vectors spanning $\mathscr{R}_{\mathrm{rep}}(t)$ by columns. Analogously, $\boldsymbol{r}_{0,\mathrm{rep}}$ represents a vector of repatoms' positions in the reference configuration. Eq. (16) basically introduces a geometric equality constraint for $\widehat{\boldsymbol{r}}$ which, upon substitution into Eq. (7), entails that the incremental energy becomes a function of $\widehat{\boldsymbol{r}}_{\mathrm{rep}}$ and $\boldsymbol{r}_{\mathrm{rep}}(t_{k-1})$, i.e.

$$\Pi^k(\widehat{\boldsymbol{r}},\widehat{\boldsymbol{z}}_{\mathrm{p}},\widehat{\boldsymbol{z}}_{\mathrm{c}};\boldsymbol{r}(t_{k-1}),\boldsymbol{z}_{\mathrm{p}}(t_{k-1}),\boldsymbol{z}_{\mathrm{c}}(t_{k-1})) = \Pi^k(\boldsymbol{\Phi}\widehat{\boldsymbol{r}}_{\mathrm{rep}},\widehat{\boldsymbol{z}}_{\mathrm{p}},\widehat{\boldsymbol{z}}_{\mathrm{c}};\boldsymbol{\Phi}\boldsymbol{r}_{\mathrm{rep}}(t_{k-1}),\boldsymbol{z}_{\mathrm{p}}(t_{k-1}),\boldsymbol{z}_{\mathrm{c}}(t_{k-1})), \tag{17}$$

reducing the number of degrees of freedom associated with the kinematic state of the system from $2\,n_{\mathrm{ato}}$ to $2\,n_{\mathrm{rep}}$, which is substantial if $n_{\mathrm{rep}} \ll n_{\mathrm{ato}}$. Minimization in (IP) with respect to $\widehat{\boldsymbol{r}} \in \mathscr{R}(t)$ then changes to a minimization over the subspace $\mathscr{R}_{\mathrm{rep}}(t)$ which, due to the linearity in (16), effectively yields a projection of the full solution to that subspace. In order to specify $\boldsymbol{\Phi}$, one usually introduces a triangulation of Ω_0 equipped with piecewise-affine shape functions with compact support (in analogy to the FE methodology, where the nodes are the repatoms). This triangulation is finely resolved (to fully recover the underlying lattice) in the region of interest and coarsely elsewhere. Evaluations of these shape functions at the positions of all atoms then provide the base vectors,

$$\boldsymbol{\Phi} = \Phi_{(2\alpha-1)(2j-1)} = \Phi_{(2\alpha)(2j)} = \varphi_{\beta_j}(\boldsymbol{r}^{\alpha}_0),\ \alpha \in N_{\mathrm{ato}},\ \beta_j \in N^{\mathrm{ato}}_{\mathrm{rep}},\ j = 1,\dots,n^{\mathrm{ato}}_{\mathrm{rep}}, \tag{18}$$

where $\beta_j = N_{\mathrm{rep}}^{\mathrm{ato}}(j)$ denotes the j-th element of the set $N_{\mathrm{rep}}^{\mathrm{ato}}$, and $\varphi_\beta(\boldsymbol{r}_0^\alpha)$ represents a shape function associated with a repatom β that is evaluated for an atom α in the undeformed configuration. In addition, we assume that the shape functions satisfy the Kronecker-delta property, i.e. $\varphi_\beta(\boldsymbol{r}_0^\gamma) = \delta^{\beta\gamma}$ for $\beta, \gamma \in N_{\mathrm{rep}}^{\mathrm{ato}}$, as well as partition-of-unity property, i.e. $\sum_{\beta \in N_{\mathrm{rep}}^{\mathrm{ato}}} \varphi_\beta(\boldsymbol{r}_0^\alpha) = 1$ for each $\alpha \in N_{\mathrm{ato}}$. Note that higher-order or meshless interpolations are possible as well, see e.g. Xiao and Yang (2007), Kwon et al. (2009), Beex et al. (2015b), or Yang and To (2015).

Similarly, we could introduce internal variables associated with repbonds $N_{\mathrm{rep}}^{\mathrm{bon}} \subseteq N_{\mathrm{bon}}$, and through interpolation represent all the remaining internal variables of the system,

$$\widehat{\boldsymbol{z}}_\bullet = \boldsymbol{\Psi} \widehat{\boldsymbol{z}}_{\bullet,\mathrm{rep}}, \tag{19}$$

where $\bullet$ stands either for "p" or "c". Eq. (19) then would constrain the admissible vector of either plastic elongations $\widehat{\boldsymbol{z}}_{\mathrm{p}}$ or cumulative plastic elongations $\widehat{\boldsymbol{z}}_{\mathrm{c}}$. This approach would, however, lead to a different technique than introduced by Beex et al. (2014c), with possible benefits in error estimation, cf. e.g. Chen et al. (2015), since the procedure treats all unknowns equally and resembles a structure-preserving Reduced-Order-Modelling method, cf. e.g. Quarteroni and Gianluigi (2014) or Fritzen et al. (2014). Some similarities with the models for bond-sliding by Beex et al. (2014d) can be observed. However, let us emphasize that in their case, the internal variables associated with sliding are attributed to nodes rather than to bonds, so that they can be approximated in the same way as the displacements. Within the virtual-power-based QC framework for lattices with plasticity, only a subset of unknowns (denoted $\widehat{\boldsymbol{z}}_{\bullet,\mathrm{sam}}$) is sought as well, but this is an assumption of the *summation* rule, yielding an approximation to incremental energy Π^k rather than a geometrical constraint, see Section 3.2 below. Equation (19) is therefore not included in further considerations and is left as a possible future challenge.

3.2. Summation

The interpolation step with piece-wise affine shape functions ensures that all atomic bonds inside triangles follow a homogeneous deformation, and therefore yields constant site energies for atoms that have all their nearest neighbours inside the same triangle, cf. Fig. 2. This observation was significantly used during the construction of summation rules briefly recalled below.

Let us express the approximation to the incremental energy defined in Eqs. (7) and (15) as

$$\Pi^k \approx \widehat{\Pi}^k = \boldsymbol{\Sigma}^{\mathsf{T}} \widehat{\boldsymbol{\pi}}, \tag{20}$$

where $\boldsymbol{\Sigma}$ in general has the form $\boldsymbol{\Sigma} = [w_1, \ldots, w_{n_{\mathrm{ato}}}]^{\mathsf{T}}$, $w_\alpha \geq 0$, and $\widehat{\boldsymbol{\pi}} = [\widehat{\pi}_1^k, \ldots, \widehat{\pi}_{n_{\mathrm{ato}}}^k]^{\mathsf{T}}$ stores all individual incremental site energies. Choosing weight factors $w_\alpha = 1$, $\alpha = 1, \ldots, n_{\mathrm{ato}}$, clearly recovers the full sum presented in (15). Introducing a set of sampling atoms S_{ato} such that $w_\alpha > 0$ for $\alpha \in S_{\mathrm{ato}}$ and $w_\beta = 0$ for $\beta \in N_{\mathrm{ato}} \backslash S_{\mathrm{ato}}$, $\# S_{\mathrm{ato}} = n_{\mathrm{sam}}^{\mathrm{ato}} \ll n_{\mathrm{ato}}$, one can rewrite (20) also as

$$\widehat{\Pi}^k = \sum_{\alpha \in S_{\mathrm{ato}}} w_\alpha \widehat{\pi}_\alpha^k. \tag{21}$$

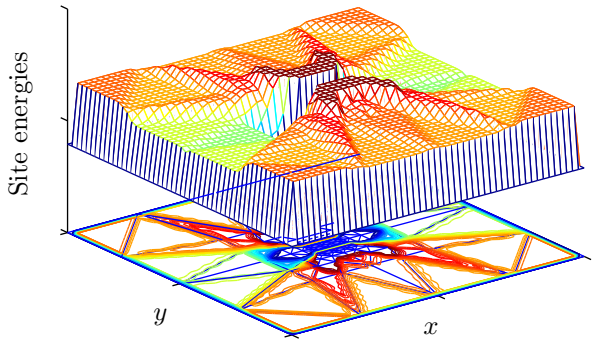

Figure 2: Site energies of a simple QC system uniformly stretched along x-axis with an inhomogeneity in the central region; energy peaks near the inhomogeneity are trimmed for visualisation purposes. In the x-y plane below the surface, contour lines are indicated for better clarity.

Analogously to sampling atoms, we introduce a set of sampling bonds, S_{bon}, $\#S_{\mathrm{bon}} = n_{\mathrm{sam}}^{\mathrm{bon}}$, defined as those bonds that are connected to all the sampling atoms S_{ato} with removed duplicity, recall Eq. (8b). The approximation of the incremental energy can then be expressed again as a sum over all sampling atoms (Eq. (21)) or as a sum over all sampling bonds (in analogy to Eq. (15)). Consequently, the dimensionality of the internal variable reduces from $2\,n_{\mathrm{bon}}$ to $2\,n_{\mathrm{sam}}^{\mathrm{bon}}$, because all variables associated with $N_{\mathrm{bon}} \setminus S_{\mathrm{bon}}$ become irrelevant. The reduced dissipative variable is denoted as $\boldsymbol{z}_{\mathrm{sam}}(t) = (\boldsymbol{z}_{\mathrm{p,sam}}(t), \boldsymbol{z}_{\mathrm{c,sam}}(t)) \in \mathscr{Z}_{\mathrm{sam}}$, where $\mathscr{Z}_{\mathrm{sam}}$ is identified with $\mathbb{R}^{2\,n_{\mathrm{sam}}^{\mathrm{bon}}}$.

Let us recall Eq. (19) and the discussion related to it. From that, it may be clear that a mapping from $\boldsymbol{z}_{\mathrm{sam}}$ back to the full solution $\boldsymbol{z}$ (i.e. $\boldsymbol{z}_{\mathrm{sam}} \to \boldsymbol{z}$ in analogy to Eq. (19)) is not necessarily unique. The reduction of the global state variable from $\boldsymbol{q}(t) = (\boldsymbol{r}(t), \boldsymbol{z}(t)) \in \mathscr{Q}$ to $\boldsymbol{q}_{\mathrm{red}}(t) = (\boldsymbol{r}_{\mathrm{rep}}(t), \boldsymbol{z}_{\mathrm{sam}}(t)) \in \mathscr{Q}_{\mathrm{red}} = \mathscr{R}_{\mathrm{rep}}(t) \times \mathscr{Z}_{\mathrm{sam}}$ is thus formed by the combination of the two QC steps that cannot be separated.

In order to compute the total energy exactly (i.e. to integrate the site energy function in Fig. 2 exactly), it is necessary to incorporate all variations along the triangles' edges. For a large triangle, the energy of only one atom site multiplied by the number of atoms within that triangle suffices to represent the plateau, whereas the atoms near the edges and in the fully resolved region must all be taken into account explicitly. This yields the so-called *exact summation rule* proposed by Beex et al. (2011), in which the explicit procedure how to compute weight factors w_α ($\alpha \in S_{\mathrm{ato}}$) and how to determine the set of sampling atoms S_{ato} can be found. Another sampling scheme focuses on the centres of the triangles and is therefore referred to as *central summation rule*, as only the plateaus and vertex atoms are sampled. See Beex et al. (2014b) or Amelang et al. (2015) for further details and Fig. 3 for a schematic representation of the two summation rules. Compared to the exact summation rule, the central summation rule is cheaper, but introduces approximation errors.

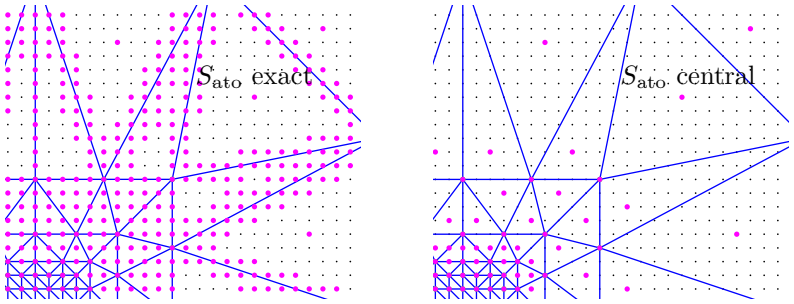

(a) exact (b) central

Figure 3: Schematic representation of the two sets of sampling atoms contained in S_{ato}; small black dots denote ordinary atom sites and larger magenta dots emphasize the sampling atoms. The triangulation is depicted in the blue colour.

4. Numerical Solution Strategies

Directly approaching (IP) with respect to both variables $\widehat{\boldsymbol{r}}$ and $\widehat{\boldsymbol{z}}$ can be cumbersome. Instead, it is relatively straightforward to perform the minimization in a staggered way, i.e. with respect to kinematic and internal variables sequentially, resulting in the AM method. This scheme appears in the literature also under names such as Block-Nonlinear Gauss–Seidel Method or Block-Coordinate Descent Method. For the original formulation the reader is referred to Csiszár and Tusnády (1984), for recent works to e.g. Byrne (2013), and for applications in variational fracture to e.g. Bourdin et al. (2000).

In the context of the variational QC method, the AM procedure needs to be applied to the incremental problem (IP) with the incremental energy defined by Eq. (7). For a fixed time step t_k, it results in the following scheme

(i) **Initialization:** $\boldsymbol{r}^0 = \boldsymbol{r}(t_{k-1})$, $\boldsymbol{z}_{\text{p}}^0 = \boldsymbol{z}_{\text{p}}(t_{k-1})$, and $\boldsymbol{z}_{\text{c}}^0 = \boldsymbol{z}_{\text{c}}(t_{k-1})$

(ii) **General iteration:** $l = 0, 1, \ldots,$ until convergence

$$\boldsymbol{r}^{l+1} = \operatorname*{arg\,min}_{\widehat{\boldsymbol{r}} \in \mathscr{R}(t_k)} \Pi^k(\widehat{\boldsymbol{r}}, \boldsymbol{z}_{\text{p}}^l, \boldsymbol{z}_{\text{c}}^l; \boldsymbol{q}(t_{k-1})), \tag{AMa}$$

$$\boldsymbol{z}_{\text{p}}^{l+1} \in \operatorname*{arg\,min}_{\widehat{\boldsymbol{z}}_{\text{p}} \in \mathbb{R}^{n_{\text{bon}}}} \Pi^k(\boldsymbol{r}^{l+1}, \widehat{\boldsymbol{z}}_{\text{p}}, \boldsymbol{z}_{\text{c}}^l; \boldsymbol{q}(t_{k-1})), \tag{AMb}$$

$$\boldsymbol{z}_{\text{c}}^{l+1} \in \operatorname*{arg\,min}_{\widehat{\boldsymbol{z}}_{\text{c}} \in \mathbb{R}^{n_{\text{bon}}}} \Pi^k(\boldsymbol{r}^{l+1}, \boldsymbol{z}_{\text{p}}^{l+1}, \widehat{\boldsymbol{z}}_{\text{c}}; \boldsymbol{q}(t_{k-1})). \tag{AMc}$$

In the first time increment, i.e. for $k = 1$, the initial condition (I) is used. Let us note that a similar scheme applies also to more general definitions of the incremental energy Π^k applicable to multi-body potentials or long-range interactions.

4.1. Full-Lattice Computation

For hardening plasticity, i.e. for $\frac{\mathrm{d}h^{\alpha\beta}(\widehat{z}_{\text{c}})}{\mathrm{d}\widehat{z}_{\text{c}}} > 0$ and $\frac{\mathrm{d}^2 h^{\alpha\beta}(\widehat{z}_{\text{c}})}{\mathrm{d}\widehat{z}_{\text{c}}^2} > 0$, the minimization in (AMc) can be performed in closed form. For arbitrary time step t_k and iteration l, the solution reads

$$z_{\text{c}}^{\alpha\beta,l+1} = z_{\text{c}}^{\alpha\beta}(t_{k-1}) + |z_{\text{p}}^{\alpha\beta,l+1} - z_{\text{p}}^{\alpha\beta}(t_{k-1})|, \ \alpha\beta = 1, \ldots, n_{\text{bon}}. \tag{23}$$

This relation follows from the bond-wise formulation of the energy in Eqs. (14a) and (15), and from the definition of the dissipation distance in Eq. (12). The minimization then decomposes into independent problems

$$z_{\mathrm{c}}^{\alpha\beta,l+1} \in \min_{\widehat{z}_{\mathrm{c}}^{\alpha\beta}\in\mathbb{R}} \widetilde{\pi}_{\alpha\beta}^{k}(r^{\alpha\beta,l+1}, z_{\mathrm{p}}^{\alpha\beta,l+1}, \widehat{z}_{\mathrm{c}}^{\alpha\beta}; \boldsymbol{q}(t_{k-1})), \;\; \alpha\beta = 1,\dots,n_{\mathrm{bon}} \tag{24}$$

solved by (23). Substituting (23) into definition (7) provides the *reduced* incremental energy, cf. e.g. Mielke and Roubíček (2015), Section 3.1.2, or Carstensen et al. (2002),

$$\Pi_{\mathrm{red}}^{k}(\widehat{\boldsymbol{r}}, \widehat{\boldsymbol{z}}_{\mathrm{p}}; \boldsymbol{q}(t_{k-1})), \tag{25}$$

and the AM algorithm simplifies to steps (AMa) – (AMb) for Π_{red}^{k}.

Continuing with step (AMa), Π_{red}^{k} is sufficiently smooth with respect to $\widehat{\boldsymbol{r}}$, so that the standard Newton's algorithm can be employed. In what follows, two nested iteration cycles will be used where l relates to AM and i to Newton's algorithm. Assuming that $\widehat{\boldsymbol{z}}_{\mathrm{p}} = \boldsymbol{z}_{\mathrm{p}}^{l}$ and, t_k and l are fixed in (25), the second-order Taylor expansion in $\widehat{\boldsymbol{r}}$, in the vicinity of $\widehat{\boldsymbol{r}}^{i}$, is applied to obtain the following stationarity conditions

$$\boldsymbol{K}^{i}(\widehat{\boldsymbol{r}}^{i+1} - \widehat{\boldsymbol{r}}^{i}) + \boldsymbol{f}^{i} = \boldsymbol{0}, \tag{26}$$

where

$$\boldsymbol{f}^{i} = \boldsymbol{f}(\widehat{\boldsymbol{r}}^{i}) = \left.\frac{\partial \Pi_{\mathrm{red}}^{k}(\widehat{\boldsymbol{r}}, \boldsymbol{z}_{\mathrm{p}}^{l}; \boldsymbol{q}(t_{k-1}))}{\partial \widehat{\boldsymbol{r}}}\right|_{\widehat{\boldsymbol{r}}=\widehat{\boldsymbol{r}}^{i}}, \tag{27a}$$

$$\boldsymbol{K}^{i} = \boldsymbol{K}(\widehat{\boldsymbol{r}}^{i}) = \left.\frac{\partial^{2} \Pi_{\mathrm{red}}^{k}(\widehat{\boldsymbol{r}}, \boldsymbol{z}_{\mathrm{p}}^{l}; \boldsymbol{q}(t_{k-1}))}{\partial \widehat{\boldsymbol{r}} \partial \widehat{\boldsymbol{r}}}\right|_{\widehat{\boldsymbol{r}}=\widehat{\boldsymbol{r}}^{i}}. \tag{27b}$$

Condition (26) supplies a system of linear equations for increments $\widehat{\boldsymbol{r}}^{i+1} - \widehat{\boldsymbol{r}}^{i}$. Iterating (26) and (27) until convergence of $||\boldsymbol{f}^{i}||_2$ then yields $\boldsymbol{r}^{l+1}$. As usual, Dirichlet boundary conditions are imposed through known increments for constrained atoms. For tying conditions, the constrained primal-dual minimization procedure is applied, cf. Section 5. We refer also to Tadmor and Miller (2011), Section 6.4.4, for similar approaches used for MS systems. The gradients $\boldsymbol{f}^{i}$ and Hessians $\boldsymbol{K}^{i}$ are provided in detail in Eqs. (A.1) – (A.4) in Appendix A for the reader's convenience.

Before dealing with the non-smooth step (AMb), the energy is again rewritten into the bond-wise form, cf. Eqs. (14a) and (15). Consequently, (AMb) can be treated in analogy to (24), i.e.

$$\begin{aligned} z_{\mathrm{p}}^{\alpha\beta,l+1} \in \min_{\widehat{z}_{\mathrm{p}}^{\alpha\beta}\in\mathbb{R}} \widetilde{\pi}_{\mathrm{red},\alpha\beta}^{k}(r^{\alpha\beta,l+1}, \widehat{z}_{\mathrm{p}}^{\alpha\beta}; \boldsymbol{q}(t_{k-1})) \iff \\ 0 \in \partial\, \widetilde{\pi}_{\mathrm{red},\alpha\beta}^{k}(r^{\alpha\beta,l+1}, z_{\mathrm{p}}^{\alpha\beta,l+1}; \boldsymbol{q}(t_{k-1})), \;\; \alpha\beta = 1,\dots,n_{\mathrm{bon}}, \end{aligned} \tag{28}$$

where ∂ denotes the subdifferential with respect to $\widehat{z}_{\mathrm{p}}^{\alpha\beta}$, cf. e.g. (Roubíček, 2005) or (Bonnans et al., 2006, Section 8.1), and $\widetilde{\pi}_{\mathrm{red},\alpha\beta}^{k}$ represents a reduced bond energy. In mechanics terms, Eq. (28) represents the Karush–Kuhn–Tucker complementarity conditions of a stretched uniform bar with isotropic hardening, and can thus be solved with the standard return-mapping algorithm described in detail e.g. in Simo and Hughes (2000), Section 1.4.2.

4.2. QC Computation

Instead of minimizing the exact incremental energy Π^k_{red}, its approximation $\widehat{\Pi}^k_{\mathrm{red}}$ in terms of the reduced variable $\boldsymbol{q}_{\mathrm{red}} \in \mathscr{Q}_{\mathrm{red}}$ is minimized in the variational QC formulation. Using the chain rule in the Taylor series expansion applied in step (AMa), recall Eqs. (17) and (21), provides the stationarity conditions

$$\boldsymbol{H}^i(\widehat{\boldsymbol{r}}^{i+1}_{\mathrm{rep}} - \widehat{\boldsymbol{r}}^{i}_{\mathrm{rep}}) + \boldsymbol{G}^i = \boldsymbol{0}, \tag{29}$$

with

$$\boldsymbol{G}^i = \boldsymbol{G}(\widehat{\boldsymbol{r}}^{i}_{\mathrm{rep}}) = \boldsymbol{\Phi}^{\mathsf{T}} \frac{\partial \widehat{\Pi}^k_{\mathrm{red}}(\widehat{\boldsymbol{r}}, \boldsymbol{z}^l_{\mathrm{p}}; \boldsymbol{q}_{\mathrm{red}}(t_{k-1}))}{\partial \widehat{\boldsymbol{r}}}\bigg|_{\widehat{\boldsymbol{r}}=\boldsymbol{\Phi}\widehat{\boldsymbol{r}}^{i}_{\mathrm{rep}}}, \tag{30a}$$

$$\boldsymbol{H}^i = \boldsymbol{H}(\widehat{\boldsymbol{r}}^{i}_{\mathrm{rep}}) = \boldsymbol{\Phi}^{\mathsf{T}} \frac{\partial^2 \widehat{\Pi}^k_{\mathrm{red}}(\widehat{\boldsymbol{r}}, \boldsymbol{z}^l_{\mathrm{p}}; \boldsymbol{q}_{\mathrm{red}}(t_{k-1}))}{\partial \widehat{\boldsymbol{r}} \partial \widehat{\boldsymbol{r}}} \boldsymbol{\Phi}\bigg|_{\widehat{\boldsymbol{r}}=\boldsymbol{\Phi}\widehat{\boldsymbol{r}}^{i}_{\mathrm{rep}}}, \tag{30b}$$

where the partial derivatives are expressed as

$$\frac{\partial \widehat{\Pi}^k_{\mathrm{red}}(\widehat{\boldsymbol{r}}, \boldsymbol{z}^l_{\mathrm{p}}; \boldsymbol{q}_{\mathrm{red}}(t_{k-1}))}{\partial \widehat{\boldsymbol{r}}} = \sum_{\alpha \in S_{\mathrm{ato}}} w_\alpha \frac{\partial \widehat{\pi}^k_{\mathrm{red},\alpha}(\widehat{\boldsymbol{r}}, \boldsymbol{z}^l_{\mathrm{p}}; \boldsymbol{q}_{\mathrm{red}}(t_{k-1}))}{\partial \widehat{\boldsymbol{r}}} = \sum_{\alpha \in S_{\mathrm{ato}}} w_\alpha \boldsymbol{f}^\alpha_{\mathrm{int}}(\widehat{\boldsymbol{r}}), \tag{31a}$$

$$\frac{\partial^2 \widehat{\Pi}^k_{\mathrm{red}}(\widehat{\boldsymbol{r}}, \boldsymbol{z}^l_{\mathrm{p}}; \boldsymbol{q}_{\mathrm{red}}(t_{k-1}))}{\partial \widehat{\boldsymbol{r}} \partial \widehat{\boldsymbol{r}}} = \sum_{\alpha \in S_{\mathrm{ato}}} w_\alpha \frac{\partial^2 \widehat{\pi}^k_{\mathrm{red},\alpha}(\widehat{\boldsymbol{r}}, \boldsymbol{z}^l_{\mathrm{p}}; \boldsymbol{q}_{\mathrm{red}}(t_{k-1}))}{\partial \widehat{\boldsymbol{r}} \partial \widehat{\boldsymbol{r}}} = \sum_{\alpha \in S_{\mathrm{ato}}} w_\alpha \boldsymbol{K}^\alpha(\widehat{\boldsymbol{r}}). \tag{31b}$$

For definitions and explicit expressions of $\boldsymbol{f}^\alpha_{\mathrm{int}}$ and $\boldsymbol{K}^\alpha$ see Eqs. (A.1) and (A.3). The converged solution of (29) is denoted by $\boldsymbol{r}^{l+1}_{\mathrm{rep}}$.

In order to minimize in (AMb), again the bond-wise version of the approximate incremental energy is employed, yielding

$$\begin{aligned} z^{\alpha\beta,l+1}_{\mathrm{p}} \in \min_{\widehat{z}^{\alpha\beta}_{\mathrm{p}} \in \mathbb{R}} \overline{w}_{\alpha\beta} \widetilde{\pi}^k_{\mathrm{red},\alpha\beta}(r^{\alpha\beta,l+1}, \widehat{z}^{\alpha\beta}_{\mathrm{p}}; \boldsymbol{q}_{\mathrm{red}}(t_{k-1})) \iff \\ 0 \in \partial\, \overline{w}_{\alpha\beta} \widetilde{\pi}^k_{\mathrm{red},\alpha\beta}(r^{\alpha\beta,l+1}, z^{\alpha\beta,l+1}_{\mathrm{p}}; \boldsymbol{q}_{\mathrm{red}}(t_{k-1})),\ \ \alpha\beta \in S_{\mathrm{bon}}, \end{aligned} \tag{32}$$

where $\overline{w}_{\alpha\beta}, \alpha\beta \in S_{\mathrm{bon}}$, denotes the weight factor associated with a bond. Because the problems in (32) are independent, the weights $\overline{w}_{\alpha\beta}$ are irrelevant (though they can be easily established from w_α) and the problem can be solved sequentially using the return-mapping algorithm in analogy to Eq. (28), but only over a subset of bonds $S_{\mathrm{bon}} \subseteq N_{\mathrm{bon}}$.

Interestingly, the resulting governing equations *exactly* coincide with those provided by Beex et al. (2014c), indicating that the virtual-power-based formulation is also variationally-consistent. Let us note that the introduction of constraints for the dissipative variables, as outlined in Eq. (19), would lead to coupled systems of equations for $\boldsymbol{z}_{\mathrm{p,rep}}$ and a different (non-local) minimization strategy would be needed instead.

Table 1: Dimensionless material and geometric parameters for all examples.

Physical parameters	Value
Young's modulus, E	1
Cross-sectional area, A	1
Yield stress, σ_0	0.01
Hardening modulus, H	10
Hardening exponent, ρ	0.5

5. Numerical Examples and Comparison

This section demonstrates the previously discussed theory for three benchmark examples, two of which were originally introduced in Beex et al. (2014c) and Beex et al. (2015b). The results will show that the energy balance (E) holds along the entire loading paths for all computed solutions. In all cases, we employ the following pair potential (in Eqs. (33) – (35), the superscripts $\alpha\beta$ are dropped for brevity)

$$\phi(\widehat{r}, \widehat{z}_\mathrm{p}) = \frac{1}{2}\frac{EA}{r_0}(\widehat{r} - r_0 - \widehat{z}_\mathrm{p})^2, \tag{33}$$

i.e. the bond stiffness reads EA/r_0, in accordance with the standard truss theory. Note that this definition corresponds to the rotated engineering deformation measure. The hardening potential reads as

$$h(\widehat{z}_\mathrm{c}) = \frac{1}{\rho+1} A\sigma_0 H r_0 \left(\frac{\widehat{z}_\mathrm{c}}{r_0}\right)^{\rho+1}, \tag{34}$$

which—by virtue of (28) and (32)—yields the power-law hardening rule in the form

$$f_Y = A\sigma_0 \left[1 + H\left(\frac{z_\mathrm{c}}{r_0}\right)^{\rho}\right]. \tag{35}$$

Here, f_Y denotes the current yield force of a bond connecting atoms α and β, whereas the initial yield force reads $f_0 = A\sigma_0$. All physical constants used throughout this section are specified in Tab. 1.[5]

5.1. Uniaxial Loading Test

As a first example a uniform loading test is presented. The domain Ω_0 occupies 100×100 lattice spacings of 1 unit length; the fully resolved system consists of $10,201$ atoms and $40,200$ bonds. A stiff region occupying 6×6 lattice spacings in the centre represents

[5] Although the choice of h made above may seem academic, note that the power hardening law (35) has been used by Beex et al. (2015a) to model the mechanical behaviour of woven fabrics.

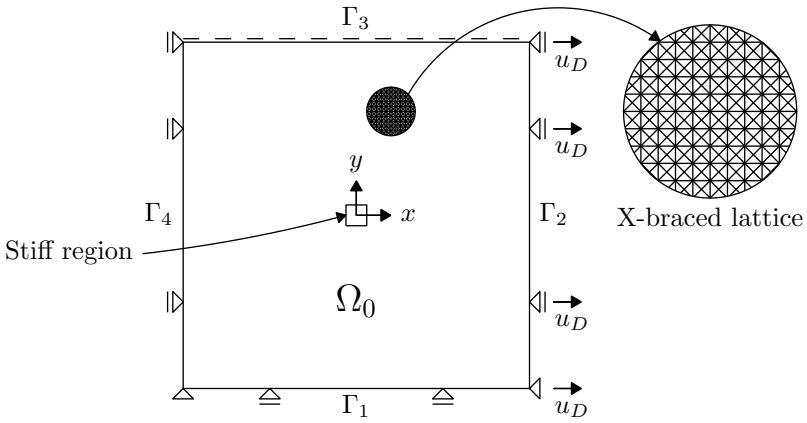

Figure 4: Scheme of the uniaxial loading test: geometry and boundary conditions.

an inhomogeneity within an otherwise homogeneous medium. The Young's modulus of the springs in the stiff domain is 100 times larger than elsewhere and the initial yield force f_0 is infinite to prevent plastic yielding in the inclusion. All bonds on the boundary $\partial\Omega_0 = \bigcup_{i=1}^{4} \Gamma_i$ (see Fig. 4), have cross-sectional areas reduced to 1/2. The boundary conditions are set according to Beex et al. (2014c), Section 4.1:

$$\begin{aligned} r_y(\Gamma_1) &= r_{0,y}(\Gamma_1) = -50, \\ r_x(\Gamma_2) &= r_{0,x}(\Gamma_2) + 10t = 50 + 10t, \ t \in [0,1], \\ r_x(\Gamma_4) &= r_{0,x}(\Gamma_4) = -50, \end{aligned} \tag{36a}$$

$$\boldsymbol{r}(\Gamma_1 \cap \Gamma_4) = \boldsymbol{r}_0(\Gamma_1 \cap \Gamma_4) = \begin{bmatrix} -50 \\ -50 \end{bmatrix},$$

$$r_y(\Gamma_3) = r_y(\Gamma_3 \cap \Gamma_4), \tag{36b}$$

where $\boldsymbol{r}(\Gamma)$ denotes the deformed configurations of all the atoms on line segment Γ ($\boldsymbol{r}^\alpha = [r_x^\alpha, r_y^\alpha]^\mathsf{T}$). Time interval $[0,1]$ is divided uniformly into 100 increments (i.e. $n_T = 100$ and $T = 1$, cf. (IP)).

The numerical example is performed for the exact and central summation rules, utilizing nine meshes; eight of them are depicted in Fig. 5 while the ninth one represents the fully-resolved lattice. In order to demonstrate the importance of the mesh quality, we use two groups of triangulations: structured "S" (Figs. 5a – 5d) and unstructured "U" (Figs. 5e – 5h), constructed such that the number of repatoms (n_{rep}) is pairwise nearly the same, see Tab. 2. For the unstructured meshes, the coarsening immediately starts outside the fully-refined region with a mild coarsening gradient. Consequently, the sizes of the fully-resolved regions differ.

Concerning the implementation of step (AMa), the Dirichlet boundary conditions (36a) are applied in the standard way. The tying condition (36b) is enforced by first collecting all atoms or repatoms on Γ_3 (except for atom $\boldsymbol{r}(\Gamma_3 \cap \Gamma_4)$) in a set N_{Γ_3}. Then, Eq. (36b) is

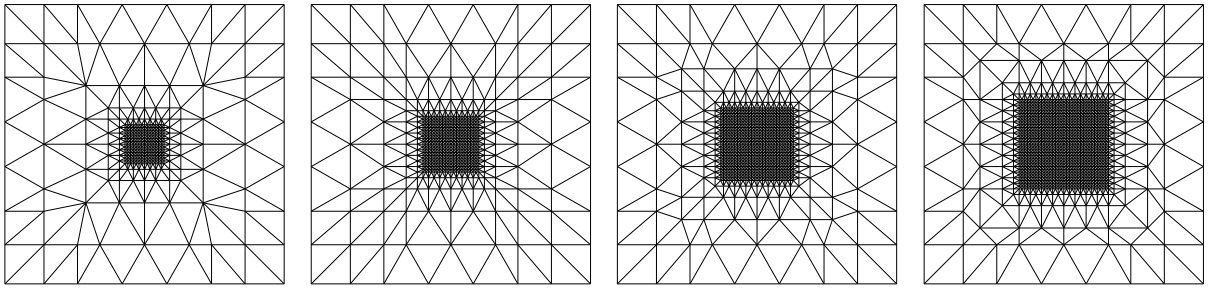

(a) S_a (b) S_b (c) S_c (d) S_d

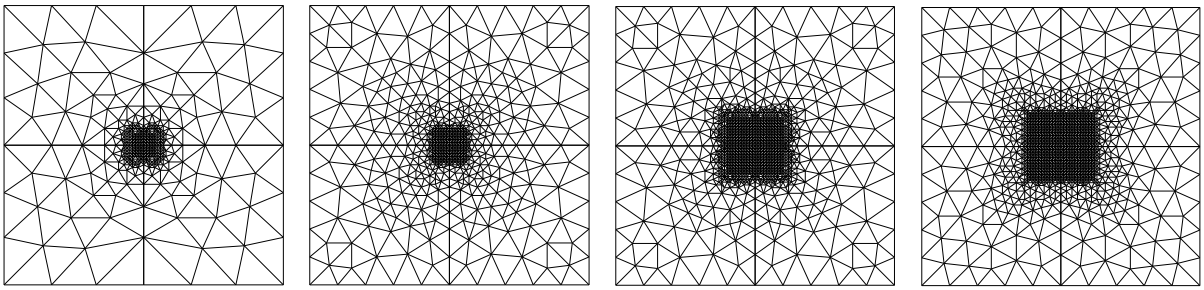

(e) U_a (f) U_b (g) U_c (h) U_d

Figure 5: Eight triangulations for the uniaxial loading test: (a) – (d) structured "S" meshes, used also in Beex et al. (2014c), and (e) – (h) unstructured "U" meshes. The sizes of the fully-resolved regions, the numbers of repatoms, sampling atoms, and sampling bonds corresponding to these meshes are provided in Tab. 2.

Table 2: Uniaxial loading test: the sizes of the fully-resolved regions "size full", numbers of repatoms n_{rep}, sampling atoms $n_{\text{sam}}^{\text{ato}}$, and sampling bonds $n_{\text{sam}}^{\text{bon}}$ for the meshes depicted in Fig. 5; "Ex" refers to the exact and "C" to the central summation rule, "S" to the structured and "U" to the unstructured meshes.

Quantity		S_a	U_a	S_b	U_b	S_c	U_c	S_d	U_d	full
size full		14×14	8×8	20×20	12×12	26×26	20×20	32×32	24×24	100×100
n_{rep}		349	337	597	537	893	969	1,277	1,113	10,201
$n_{\text{sam}}^{\text{ato}}$	Ex	5,113	5,621	5,425	8,209	5,889	8,169	6,217	8,161	10,201
	C	597	593	929	1,193	1,245	1,541	1,697	1,875	
$n_{\text{sam}}^{\text{bon}}$	Ex	25,389	27,076	26,814	36,360	28,373	36,288	29,474	36,504	40,200
	C	3,492	3,536	5,076	7,636	6,482	8,544	8,396	10,388	

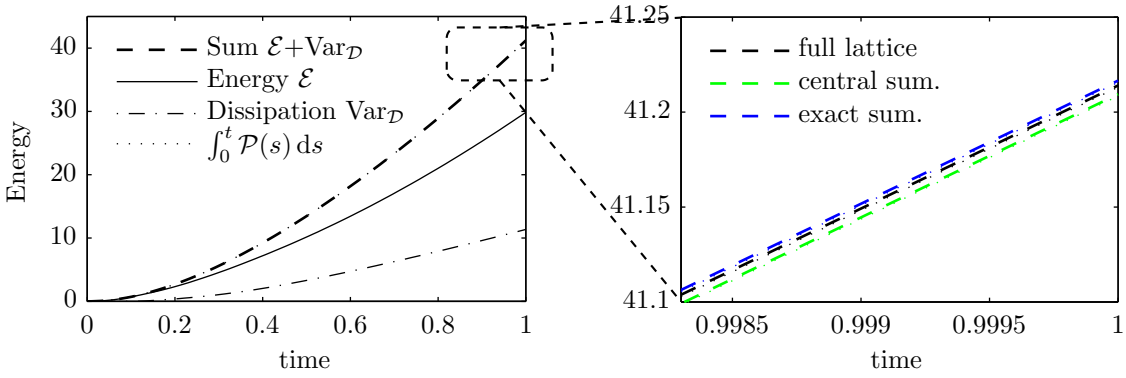

(a) energy evolutions (b) zoom

Figure 6: Results for the uniaxial loading test: (a) total energy evolution paths for all meshes and both summation rules, (b) zoom of only mesh $\mathrm{S_a}$ (Fig. 5a) for the exact and central summation rule.

rewritten as

$$r_y(\Gamma_3 \cap \Gamma_4) - r_y^\alpha = 0,\ \alpha \in N_{\Gamma_3}, \tag{37}$$

which are globally assembled to

$$\boldsymbol{C}\boldsymbol{r} = \boldsymbol{0}, \tag{38}$$

and imposed by Lagrange multipliers, i.e. by the primal-dual formulation. This yields an iterative solution of saddle-point problems (cf. Bonnans et al. (2006), Section 14), that reads

$$\begin{bmatrix} \boldsymbol{K}^i & \boldsymbol{C}^\mathsf{T} \\ \boldsymbol{C} & \boldsymbol{0} \end{bmatrix} \begin{bmatrix} \widehat{\boldsymbol{r}}^{i+1} - \widehat{\boldsymbol{r}}^i \\ \widehat{\boldsymbol{\lambda}}^{i+1} \end{bmatrix} = - \begin{bmatrix} \boldsymbol{f}^i \\ \boldsymbol{B}^i \end{bmatrix}, \quad \boldsymbol{B}^i = \boldsymbol{C}\widehat{\boldsymbol{r}}^i, \tag{39}$$

for time step t_k and AM iteration l, providing us with $\boldsymbol{r}^{l+1}$ and $\boldsymbol{\lambda}^{l+1}$ upon convergence. For QC systems, $\boldsymbol{K}^i$ is replaced with $\boldsymbol{H}^i$ and $\widehat{\boldsymbol{r}}^i$ with $\widehat{\boldsymbol{r}}^i_{\mathrm{rep}}$.

The energy profiles corresponding to the loading program (36) for all the meshes and both summation rules are depicted in Fig. 6a. Here, we notice that the curves corresponding to the individual solutions are identical and that the errors are extremely small. Moreover, we can check that all solutions satisfy the energy balance (E) along the entire loading path, since the thin dotted line corresponding to $\int_0^t \mathcal{P}(s)\,\mathrm{d}s$ lies on top of the thick dashed line representing $\mathcal{E} + \mathrm{Var}_\mathcal{D}$. Upon zooming in (Fig. 6b, where only the results for the mesh $\mathrm{S_a}$ are presented for clarity), we observe that the exact summation rule increases the system's energy with respect to the full lattice simulation, whereas the central summation rule causes the energy to be slightly lower. This behaviour is not surprising as the overall energy increases when the geometric constraints of the QC system are introduced (while using the exact summation rule). Further, since the site energies of atoms lying near the triangles' edges are higher compared to internal atoms (recall Fig. 2), the approximate energy for the central summation rule is slightly lower.

Because the exact and approximate energy profiles are indistinguishable by the naked eye, we introduce a relative error measure $L^2([0,1])$ for $\mathcal{E}(t), \mathrm{Var}_\mathcal{D}(t)$, and $\mathcal{E}(t) + \mathrm{Var}_\mathcal{D}(t)$.

Namely,

$$\varepsilon_{\widetilde{\square}} = \frac{||\square_{\mathrm{QC}} - \square_{\mathrm{full}}||_{L^2}}{||\square_{\mathrm{full}}||_{L^2}}, \tag{40}$$

where $\square$ either stands for $\mathcal{E}(t), \mathrm{Var}_{\mathcal{D}}(t)$, or $\mathcal{E}(t) + \mathrm{Var}_{\mathcal{D}}(t)$, and $\widetilde{\square}$ stands for $\mathcal{E}, \mathrm{Var}_{\mathcal{D}}$, or $\mathcal{E} + \mathrm{Var}_{\mathcal{D}}$. The subscript "QC" denotes results obtained from the QC simulations, whereas the subscript "full" represents the results computed for the fully-resolved system. The error measure $\varepsilon_{\widetilde{\square}}$ is presented for the various meshes in Fig. 7. We further distinguish between the error due to interpolation (denoted as "Int.") and the total error due to interpolation plus summation (denoted as "Tot."). Thus, "Int." relates to the error obtained for the exact summation rule, whereas "Tot." relates to the error obtained for the central summation rule. The largest value amounts to 1.43×10^{-3} and corresponds to the dissipation $\mathrm{Var}_{\mathcal{D}}$, cf. Fig. 7b. Whilst the error due to interpolation behaves in a reasonable way, i.e. decreases with an increasing dimension of the projection basis, the interpolation plus summation error surprisingly behaves in the opposite way (see Fig. 7), i.e. increases with an increasing number of sampling atoms. Since the total error is dominated by summation, this behaviour can be related to the mesh topology. Namely, to the number of triangles for which the central sampling atom and all its neighbours are not contained in the same triangle.[6] Such a conjecture is supported by the perfect match between the total error profiles in Fig. 7c and the mesh characteristics in Fig. 8. Numerically quantified, the Pearson's correlation coefficient for these data amounts to 0.998 (structured mesh) and 0.963 (unstructured mesh). This result supports the idea of a direct transition between the fully-resolved and interpolated regions, or motivates the use of rapid mesh coarsening rather than a mild one. On the other hand, the overall error is so small that this behaviour can also be deemed singular. Finally, let us note that while the energy errors (global error measures) are negligible, the relative errors of the internal variables (local error measures) are still noticeable, cf. Beex et al. (2014c), Section 4.3. But this is consistent with one's expectations as the QC aims to closely approximate the global incremental energy Π^k, recall Section 3.2.

Concerning the mesh types, we conclude from Fig. 7 that the performance in terms of the interpolation error is nearly the same, though the unstructured meshes are slightly more accurate. In terms of the total error, however, the structured meshes perform evidently better. The structured ones are also more efficient, as for them the corresponding numbers of sampling atoms ($n_{\mathrm{sam}}^{\mathrm{ato}}$) and sampling bonds ($n_{\mathrm{sam}}^{\mathrm{bon}}$) are systematically lower, see Tab. 2. Recall that the numbers of repatoms (n_{rep}) remain comparable. Such behaviour can again be related to the mesh topology and the mesh coarsening gradient. Combined results from Fig. 7 and Tab. 2 reveal that by accepting energy errors up to 2 %, the number of degrees of freedom reduces up to the factor of 30. In the case of sampling atoms, the reduction is up to the factor of 17.

The highly accurate energy reconstruction of the QC method for the uniform loading test is attributed to two aspects. First, the (plastic) deformation field is more or less piecewise

[6] Note that in accordance with the QC convention, a triangular element is considered as a closed set. Consequently, the atoms lying on element's edges or vertices are contained in that triangle.

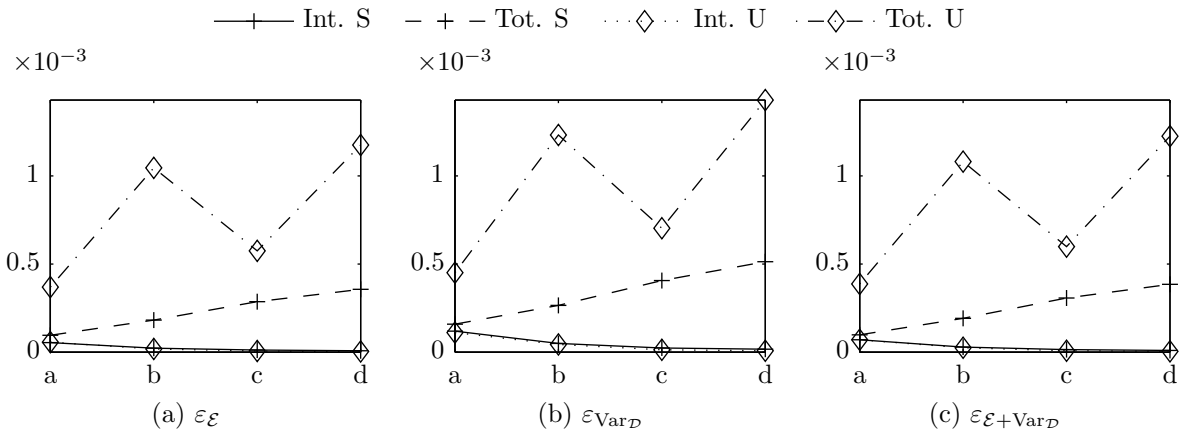

(a) $\varepsilon_{\mathcal{E}}$ (b) $\varepsilon_{\mathrm{Var}_{\mathcal{D}}}$ (c) $\varepsilon_{\mathcal{E}+\mathrm{Var}_{\mathcal{D}}}$

Figure 7: Results for the uniaxial loading test: relative error $\varepsilon_{\widetilde{\square}}$ (Eq. (40)) for the meshes presented in Fig. 5. "Int." relates to interpolation (exact summation rule) and "Tot." to interpolation plus summation (central summation rule).

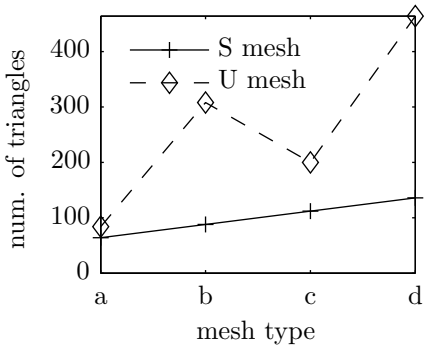

Figure 8: Results for the uniaxial loading test: number of triangles for which the central sampling atoms do not have all their neighbours within the same triangle; meshes from Fig. 5 used.

constant over the deformed domain $\Omega(t)$. Hence, it is well captured by constant approximations within triangles. Second, perturbations near the inhomogeneity are resolved accurately by all employed meshes. Consequently, the summation error outweighs the interpolation error. These two reasons and the example presented in Beex et al. (2015b), Sections 4.2 and 5.2 motivate the following test, in which the deformation field due to bending is linear rather than constant and more pronounced interpolation errors are expected.

5.2. Pure Bending Test

In this example, the domain Ω_0 is exposed to pure bending around the z-axis, cf. Fig. 9. An inhomogeneity of 6×6 lattice spacings is situated at the bottom edge, in which the trusses have a 100-times higher Young's modulus and an infinite initial yield force f_0 prevents plastic yielding. The entire domain occupies 200×100 lattice units and comprises $20,301$ atoms connected by $80,300$ bonds. The boundary conditions for $\partial\Omega_0 = \bigcup_{i=1}^{4} \Gamma_i$ read as follows

$$r_x(\Gamma_4) = r_{0,x}(\Gamma_4) = -100,$$
$$\boldsymbol{r}(\Gamma_1 \cap \Gamma_4) = \boldsymbol{r}_0(\Gamma_1 \cap \Gamma_4) = \begin{bmatrix} -100 \\ -50 \end{bmatrix}, \tag{41a}$$
$$\frac{r_x^{\alpha_{j+1}} - r_x^{\alpha_j}}{r_y^{\alpha_{j+1}} - r_y^{\alpha_j}} = \tan\theta, \;\; j = 1, \dots, n_{\Gamma_2} - 1, \tag{41b}$$

where we have collected n_{Γ_2} atoms or repatoms on Γ_2 in the set N_{Γ_2}; note that $\alpha_j = N_{\Gamma_2}(j)$ denotes the j-th element of N_{Γ_2}. All atoms in N_{Γ_2} are sorted from bottom to top, i.e. $r_y^{\alpha_{j+1}} > r_y^{\alpha_j}$, and hence, $\boldsymbol{r}^{\alpha_1} = \boldsymbol{r}(\Gamma_1 \cap \Gamma_2)$ and $\boldsymbol{r}^{\alpha_{n_{\Gamma_2}}} = \boldsymbol{r}(\Gamma_2 \cap \Gamma_3)$. Condition (41b) therefore requires that $\boldsymbol{r}(\Gamma_2)$ follows a straight line that is allowed to freely move in space and has a slope θ, cf. Fig. 9b. Note that atoms can slide frictionlessly along this line but cannot move in the perpendicular direction. Equation (41b) can then be rewritten as

$$r_x^{\alpha_{j+1}} - r_x^{\alpha_j} + (r_y^{\alpha_j} - r_y^{\alpha_{j+1}}) \tan\theta = 0, \;\; j = 1, \dots, n_{\Gamma_2} - 1, \tag{42}$$

and globally assembled as

$$\boldsymbol{C}(\theta)\boldsymbol{r} = \boldsymbol{0}, \tag{43}$$

in analogy to Eqs. (37) and (38). Since the constraints now depend on $\theta(t)$ through Eq. (44) below, matrix $\boldsymbol{C}$ changes for each time step t_k. To accomodate this, $\boldsymbol{C}$ is replaced by $\boldsymbol{C}_k = \boldsymbol{C}(\theta(t_k))$ in Eq. (39). The overall deformation process is finally parametrized as

$$\theta(t) = \frac{\pi}{6}\, t, \;\; t \in [0, 1], \tag{44}$$

and the time interval is divided into 100 uniform increments (i.e. $n_T = 100$, $T = 1$).

The numerical example is again studied for the two summation rules, but now only for five unstructured meshes. Four of them are shown in Fig. 10, the fifth one represents the full lattice. The corresponding numbers of atoms, repatoms, and sampling bonds can be found in Tab. 3.

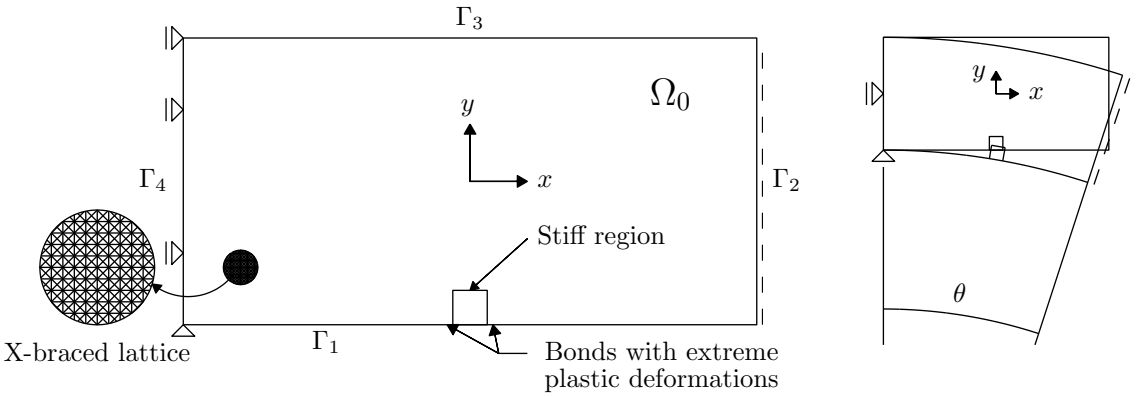

(a) geometry (b) deformed state

Figure 9: Scheme of the pure bending test: geometry, boundary conditions, and deformed state.

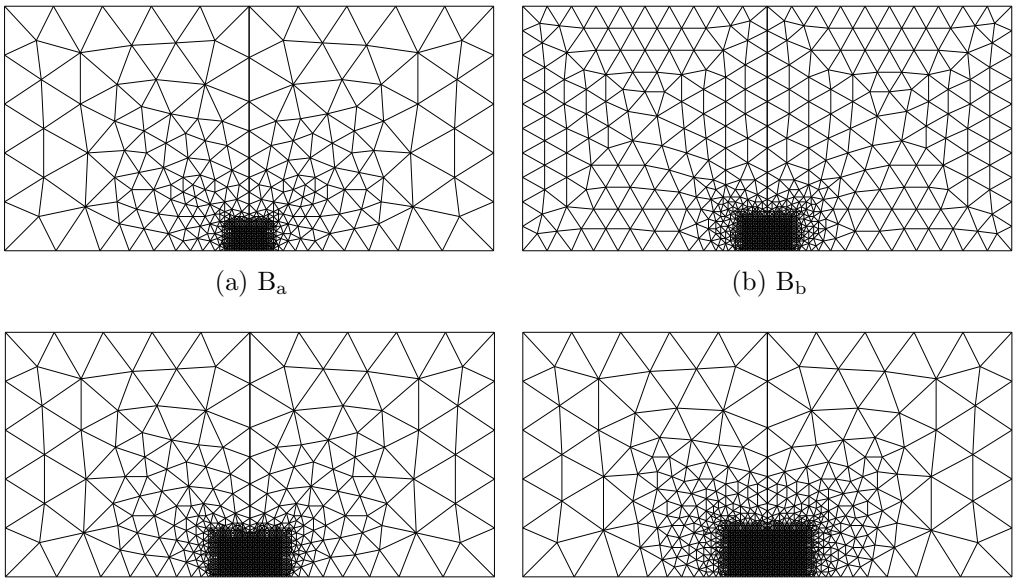

(a) B_a (b) B_b

(c) B_c (d) B_d

Figure 10: The four triangulations for the pure bending test; the sizes of the fully-resolved regions, the numbers of repatoms, sampling atoms, and sampling bonds are presented in Tab. 3.

Table 3: Data for the pure bending test: the sizes of the fully-resolved regions "size full", numbers of repatoms n_{rep}, sampling atoms $n_{\text{sam}}^{\text{ato}}$, and sampling bonds $n_{\text{sam}}^{\text{bon}}$ for the meshes depicted in Fig. 10; "Ex" refers to the exact and "C" to the central summation rule.

Quantity		B_a	B_b	B_c	B_d	full
size full		14×10	20×13	26×16	32×19	200×100
n_{rep}		507	812	894	1,194	20,301
$n_{\text{sam}}^{\text{ato}}$	Ex	10,709	13,989	10,693	11,301	20,301
	C	941	1,558	1,342	1,872	
$n_{\text{sam}}^{\text{bon}}$	Ex	51,094	66,990	51,136	52,432	80,300
	C	5,789	9,574	7,215	10,120	

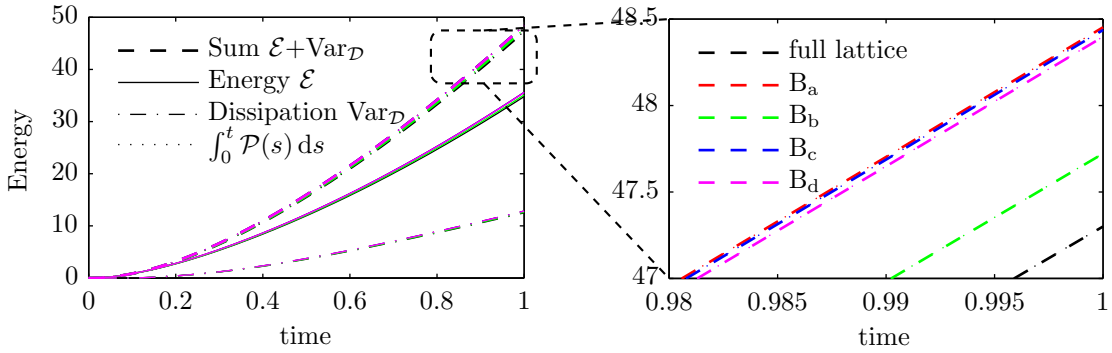

(a) exact summation rule (b) zoom

Figure 11: Results for the pure bending test: (a) total energy evolution paths, (b) zoom; the different meshes from Fig. 10 using the exact summation rule are compared to the full-lattice solution.

The energy evolution paths for all meshes are shown in Fig. 11 for the exact summation rule, and in Fig. 12 for the central summation rule. Here, the differences between the solutions are more pronounced compared to the previous example, though they are still quite small. The results show that the energy equality (E) holds again. Upon closer inspection, we notice that the interpolation error (Fig. 11b) is smallest for mesh B_b, which has the smallest overall element size. So the error is dominated by the limitation of constant strain triangles to capture bending, and is almost insensitive to the size of the fully-resolved region. Instead of refining the triangulation in the coarse part of the domain, an alternative approach for decreasing the interpolation error would be to use higher-order approximations, as shown e.g. in Beex et al. (2015b). Furthermore, the total error due to interpolation and summation (Fig. 12b) is smaller than the interpolation error alone, meaning that the two errors partially compensate.

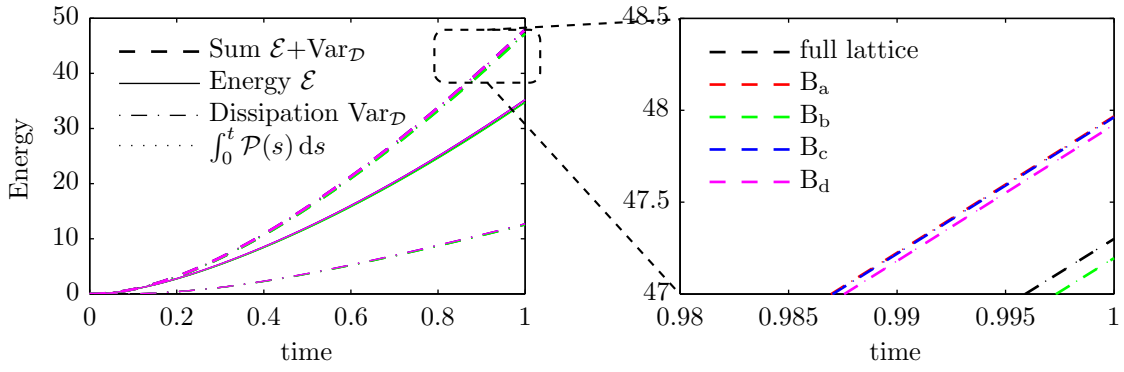

(a) central summation rule (b) zoom

Figure 12: Results for the pure bending test: (a) energy evolution paths, (b) zoom; the different meshes from Fig. 10 using the central summation rule are compared to the full-lattice solution.

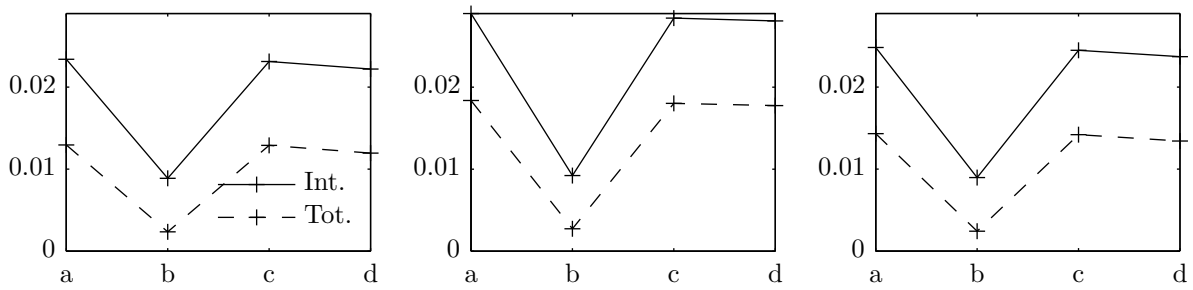

(a) $\varepsilon_\mathcal{E}$ (b) $\varepsilon_{\mathrm{Var}_\mathcal{D}}$ (c) $\varepsilon_{\mathcal{E}+\mathrm{Var}_\mathcal{D}}$

Figure 13: Results for the pure bending test: relative errors $\varepsilon_{\widetilde{\square}}$ defined in Eq. (40) for the various meshes depicted in Fig. 10. "Int." relates to interpolation (exact summation rule) and "Tot." to interpolation plus summation (central summation rule).

The relative error $\varepsilon_{\widetilde{\square}}$, defined in Eq. (40), can be found in Fig. 13 for the four meshes and the two summation rules. The best agreement achieved for mesh B$_b$ is due to the finer mesh resolution over the entire domain Ω; the largest error amounts to 28.98×10^{-3} attained for mesh B$_a$, for dissipation Var$_\mathcal{D}$ presented in Fig. 13b. Comparing the increase in the number of repatoms with respect to error, we conclude from Fig. 13 and Tab. 3 that by accepting an energy error below 3 %, we gain a reduction in the number of degrees of freedom up to the factor of 40, and in the number of sampling atoms up to the factor of 22. The dependency of the error in Fig. 13 on the mesh topology is more complicated than in the previous example. Specifically, the Pearson's correlation coefficient between the number of triangles with central sampling atoms that do not have all the neighbours in the same triangle and the "Tot." error in Fig. 13c drops to -0.051, indicating no dependence.

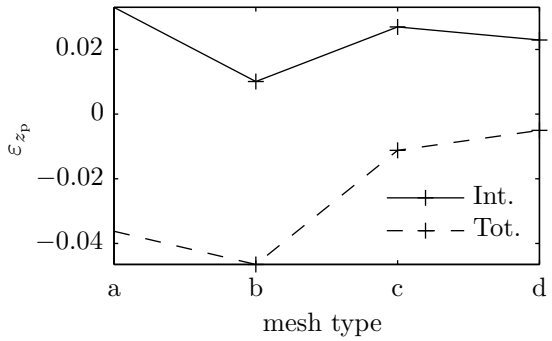

Figure 14: Results for the pure bending test: relative error $\varepsilon_{z_\mathrm{p}}(t=1)$ defined in Eq. (45) for various meshes depicted in Fig. 10. "Int." relates to interpolation (exact summation rule) and "Tot." to interpolation plus summation (central summation rule).

Finally, the following quantity is examined

$$\varepsilon_{z_\mathrm{p}}(t) = \frac{||\boldsymbol{z}^{\mathrm{QC}}_{\mathrm{p,sam}}(t)||_\infty - ||\boldsymbol{z}^{\mathrm{full}}_{\mathrm{p}}(t)||_\infty}{||\boldsymbol{z}^{\mathrm{full}}_{\mathrm{p}}(t)||_\infty}, \tag{45}$$

measuring the relative error between full-lattice "full" and approximate "QC" solutions for extreme plastic deformations attained at Γ_1 alongside the inhomogeneity, cf. Fig. 9a. Recall that for some $\boldsymbol{z} \in \mathbb{R}^n$, the norm in Eq. (45) reads as $||\boldsymbol{z}||_\infty = \max\{|z_1|, \ldots, |z_n|\}$. Quantity $\varepsilon_{z_\mathrm{p}}(t=1)$ is presented for the different meshes and summation rules in Fig. 14. It can be seen that the size of the fully resolved region has again less influence on the error than the mesh refinement in the coarse domain. Because the interpolation increases the energy of the system and the summation slightly underestimates it, the two effects again cancel each other to some extent. Notice that this does not hold for mesh $\mathrm{B_b}$, for which the summation error dominates.

5.3. Indentation Test

In the final example, we consider a homogeneous X-braced lattice occupying a rectangular domain Ω_0 of 256×128 lattice spacings, containing $33,153$ atoms and $131,456$ bonds, cf. Fig. 15. In accordance with the previous examples, the lattice spacings in both directions are of unit length. The boundary conditions are prescribed as

$$\boldsymbol{r}(\Gamma_1 \cup \Gamma_2 \cup \Gamma_4) = \boldsymbol{r}_0(\Gamma_1 \cup \Gamma_2 \cup \Gamma_4), \tag{46}$$

and the remaining part of the boundary, Γ_3, is left free for potential frictionless contact with a rigid circular indenter. The indenter is characterized by its radius, $r_\mathrm{I} = 32$, and centre

$$\boldsymbol{c}_\mathrm{I}(t) = \begin{bmatrix} 0 \\ r_{y,0}(\Gamma_3) + r_\mathrm{I}(1 - t/4) \end{bmatrix}, \quad t \in [0,1]. \tag{47}$$

The time interval is again uniformly divided into 100 increments, i.e. $n_T = 100$ and $T = 1$. The inequality constraints associated with contact between the lattice and the indenter read

$$g_j(\boldsymbol{r}^{\alpha_j}) = r_{\mathrm{I}}^2 - ||\boldsymbol{r}^{\alpha_j} - \boldsymbol{c}_{\mathrm{I}}||_2^2 \leq 0, \quad j = 1, \ldots, n_{\Gamma_3}, \tag{48}$$

where we have collected the n_{Γ_3} atoms or repatoms lying on Γ_3 part of the boundary in the set N_{Γ_3}; recall that $\alpha_j = N_{\Gamma_3}(j)$ is the j-th element of N_{Γ_3}. These constraints are incorporated through the primal-dual formulation as before, Bonnans et al. (2006). To that purpose, we iteratively form a set of active constraints

$$\mathcal{A} = \big\{ j \in \{1, \ldots, n_{\Gamma_3}\} \,|\, g_j(\boldsymbol{r}^{\alpha_j}) \geq 0 \text{ and associated Lagrange multiplier } \lambda_j \geq 0 \big\}. \tag{49}$$

For inactive constraints, i.e. for $j \in \{1, \ldots, n_{\Gamma_3}\} \backslash \mathcal{A}$, the associated $\lambda_j = 0$. For all active constraints $j \in \mathcal{A}$, the inequality conditions (48) are enforced as equality constraints

$$\boldsymbol{g}(\boldsymbol{r}) = \boldsymbol{0} \tag{50}$$

and implemented using Eq. (39), where we substitute

$$\begin{aligned} \boldsymbol{K}^i = \boldsymbol{K}(\widehat{\boldsymbol{r}}^i) &= \left. \frac{\partial^2 \Pi^k_{\mathrm{red}}}{\partial \widehat{\boldsymbol{r}} \partial \widehat{\boldsymbol{r}}} \right|_{\widehat{\boldsymbol{r}} = \widehat{\boldsymbol{r}}^i} + \sum_{j \in \mathcal{A}} \widehat{\lambda}_j \left. \frac{\partial^2 g_j(\widehat{\boldsymbol{r}}^{\alpha_j})}{\partial \widehat{\boldsymbol{r}} \partial \widehat{\boldsymbol{r}}} \right|_{\widehat{\boldsymbol{r}} = \widehat{\boldsymbol{r}}^i, \widehat{\boldsymbol{\lambda}} = \widehat{\boldsymbol{\lambda}}^i}, \\ \boldsymbol{C}^i = \boldsymbol{C}(\widehat{\boldsymbol{r}}^i) &= \left(\frac{\partial \boldsymbol{g}(\widehat{\boldsymbol{r}})}{\partial \widehat{\boldsymbol{r}}} \right)^{\mathsf{T}} \Bigg|_{\widehat{\boldsymbol{r}} = \widehat{\boldsymbol{r}}^i}, \quad \boldsymbol{B}^i = \boldsymbol{g}(\widehat{\boldsymbol{r}}^i). \end{aligned} \tag{51}$$

Because the tangent $\boldsymbol{C}(\widehat{\boldsymbol{r}}^i)$ now depends on $\widehat{\boldsymbol{r}}^i$, it must be updated every Newton iteration, in contrast to the previous two examples. Possible violations of the inequality constraints are checked after convergence of Newton's algorithm. If a change in $\mathcal{A}$ occurs, Newton's algorithm is called again and the entire procedure is repeated until convergence of $\mathcal{A}$. The same strategy applies also to QC systems.

The numerical example is studied for the exact and central summation rule and again for five meshes. Four of them are depicted in Fig. 16, whereas the fifth represents the full lattice. Two meshes are regular and two irregular, pairwise with nearly the same number of repatoms and identical sizes of the fully-resolved regions, cf. Tab. 4.

A detailed view of the deformed configuration at $t = 1$ for the full lattice solution can be found in Fig. 17a. Note that only one half is shown thanks to symmetry. The dissipation localizes below the indenter through a plastic shear band, indicated in red. The reaction force of the indenter is presented in Fig. 17b, where we notice a good agreement between the QC simulations with the full lattice solution, especially for structured meshes $\mathrm{I_a}$ and $\mathrm{I_b}$. Because the differences between the solid and dashed lines are negligible, we can conclude that the choice of the summation rule does not influence the results and the errors are dominated by interpolation, similarly to the pure bending test in Section 5.2.

The energy evolution profiles are presented in Fig. 18 for the exact, and in Fig. 19 for the central summation rule. The results show that the energy balance (E) holds in all cases, and that the differences between the two summation rules are practically negligible—as already suggested by Fig. 17b. Upon closer investigation (in Figs 18b and 19b), a better performance of the structured meshes compared to the unstructured ones can be observed again.

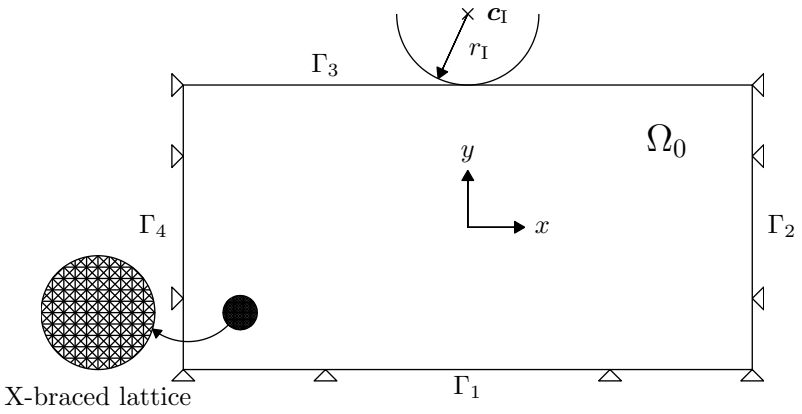

Figure 15: Scheme of the indentation test: geometry and boundary conditions.

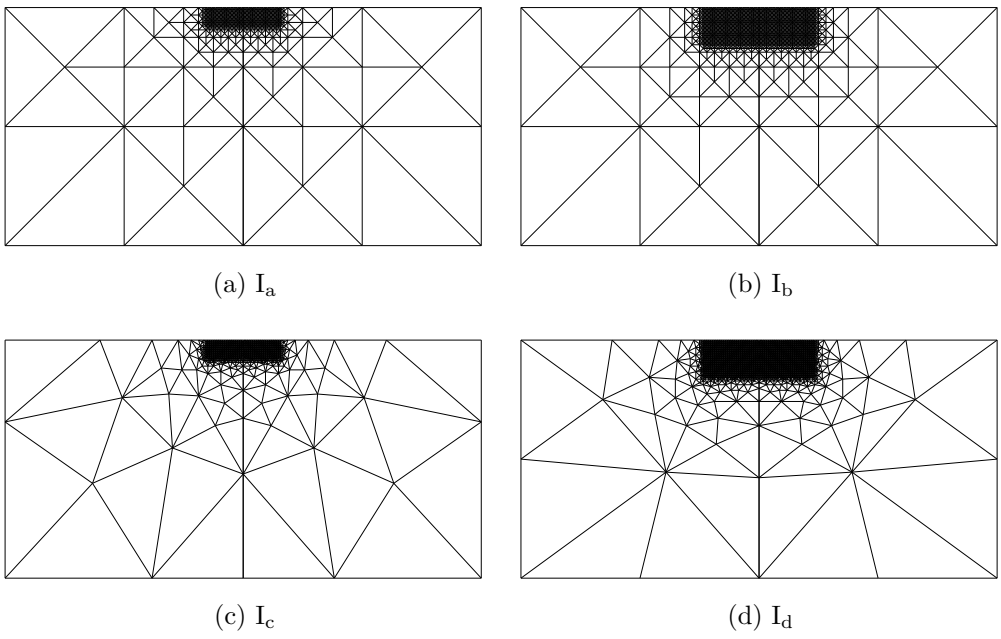

(a) I_a (b) I_b

(c) I_c (d) I_d

Figure 16: The four triangulations for the indentation test; the sizes of the fully-resolved regions, the numbers of repatoms, sampling atoms, and sampling bonds are presented in Tab. 4.

Table 4: Data for the indentation test: the sizes of the fully-resolved regions "size full", the numbers of repatoms n_{rep}, sampling atoms $n_{\text{sam}}^{\text{ato}}$, and sampling bonds $n_{\text{sam}}^{\text{bon}}$ for the meshes depicted in Fig. 16; "Ex" refers to the exact and "C" to the central summation rule.

Quantity		I_a	I_b	I_c	I_d	full
size full		40×10	60×20	40×10	60×20	256×128
n_{rep}		603	1,487	617	1,510	33,153
$n_{\text{sam}}^{\text{ato}}$	Ex	6,249	7,383	7,531	8,771	33,153
	C	876	1,857	818	1,807	
$n_{\text{sam}}^{\text{bon}}$	Ex	32,066	36,746	36,388	41,224	131,456
	C	4,300	8,352	3,922	8,153	

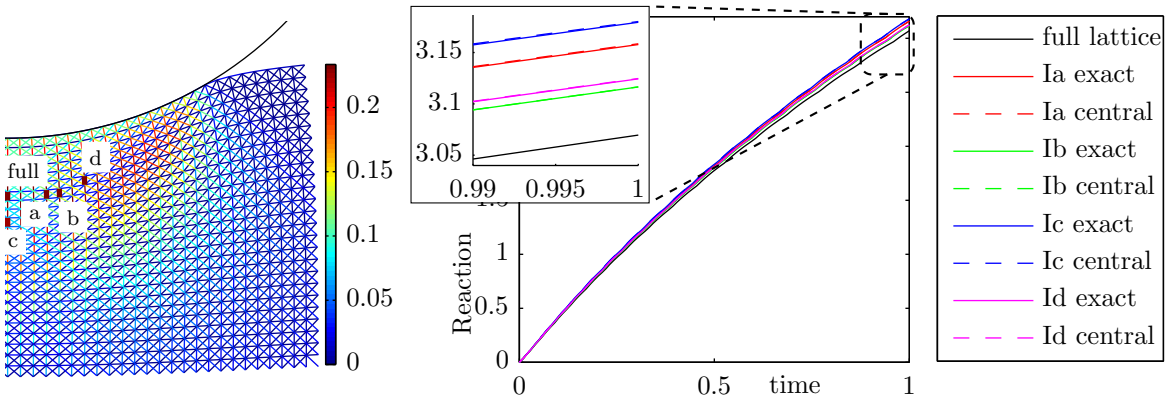

(a) $\boldsymbol{z}_{\text{c}}(t=1)$ on deformed state

(b) vertical reaction force of the indenter

Figure 17: Results for the indentation test: (a) close view of deformed configuration and the cumulative plastic slips in individual bonds for the full lattice solution, and (b) the vertical reaction force of the indenter.

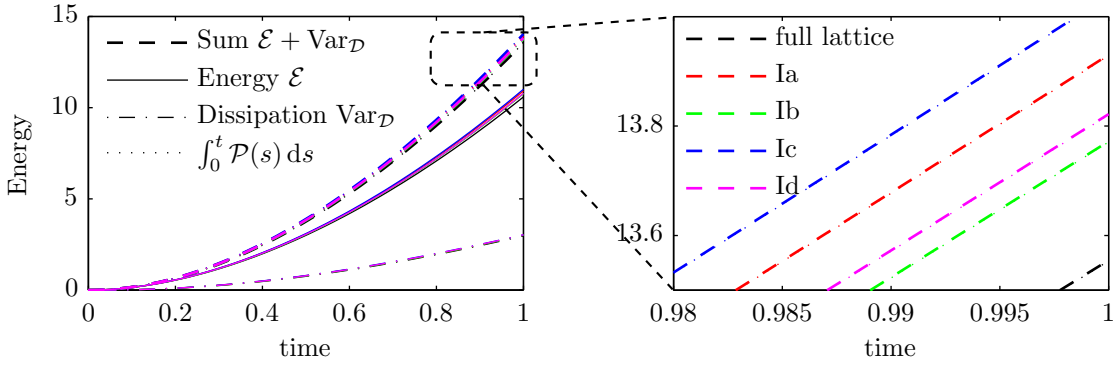

(a) exact summation rule

(b) zoom

Figure 18: Results for the indentation test: (a) total energy evolution paths, (b) zoom; the different meshes from Fig. 16 using the exact summation rule are compared to the full-lattice solution.

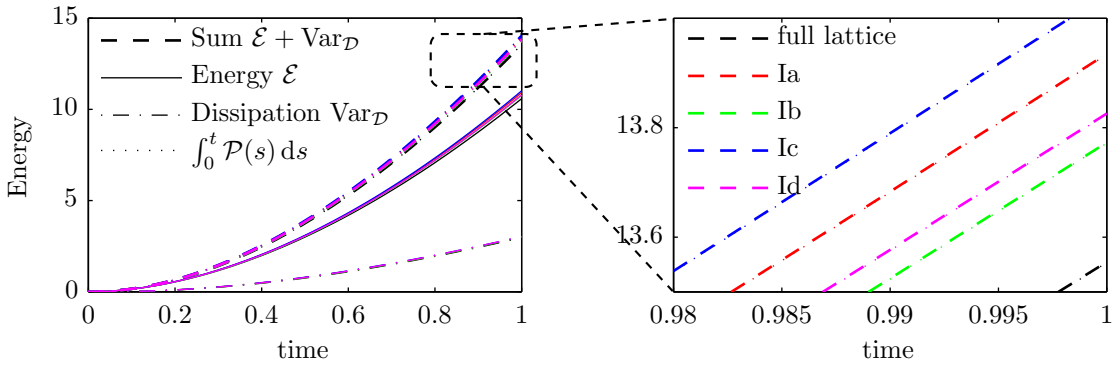

(a) central summation rule (b) zoom

Figure 19: Results for the indentation test: (a) energy evolution paths, (b) zoom; the different meshes from Fig. 16 using the central summation rule are compared to the full-lattice solution.

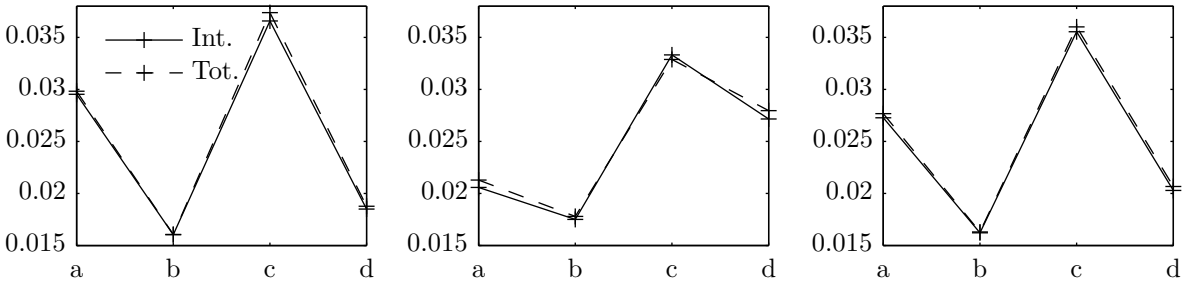

(a) $\varepsilon_\mathcal{E}$ (b) $\varepsilon_{\mathrm{Var}_\mathcal{D}}$ (c) $\varepsilon_{\mathcal{E}+\mathrm{Var}_\mathcal{D}}$

Figure 20: Results for the indentation test: relative errors $\varepsilon_{\widetilde{\square}}$ defined in Eq. (40) for the various meshes depicted in Fig. 16. "Int." relates to interpolation (exact summation rule) and "Tot." to interpolation plus summation (central summation rule).

Fig. 20 shows the energy errors $\varepsilon_{\widetilde{\square}}$ of Eq. (40) for all systems. Here we see that the best agreement with the solution of the full lattice is obtained using regular fine mesh $\mathrm{I_b}$, whereas the largest error is obtained for unstructured coarse mesh $\mathrm{I_c}$. Because the total error is dominated by the interpolation, no significant correlation between the number of triangles with central sampling atoms that do not have all the neighbours in the same triangle (Fig. 21b) and the "Tot." error (Fig. 20c) is observed. Pearson's correlation coefficient amounts to -0.198 in this case. For the summation error itself (i.e. "Tot." minus "Int." line in Fig. 20c), the correlation increases to 0.266, indicating only a mild dependence. By committing errors in energies of less than 4 %, we achieve a reduction up to a factor of 50 in terms of the number of degrees of freedom. The computational gain in terms of the number of sampling atoms is around a factor of 40.

Finally, Fig. 21a shows the local error $\varepsilon_{z_\mathrm{p}}(t=1)$ of Eq. (45). These results confirm that the size of the fully resolved region significantly influences the accuracy, whereas the choice of the summation rule has little effect on the local errors, except for mesh $\mathrm{I_c}$. Let us emphasize,

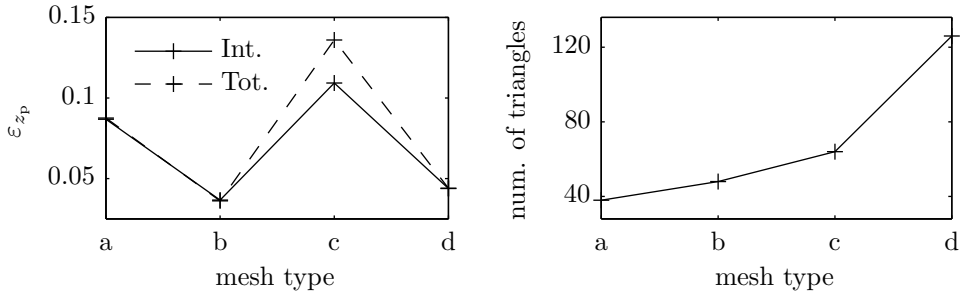

(a) $\varepsilon_{z_p}(t=1)$ (b) mesh characteristics

Figure 21: Results for the indentation test. (a) Relative error $\varepsilon_{z_p}(t=1)$ defined in Eq. (45). "Int." relates to interpolation (exact summation rule) and "Tot." to interpolation plus summation (central summation rule). (b) The number of triangles for which the central sampling atoms do not have all their neighbours within the same triangle. The meshes from Fig. 16 are used.

however, that although the errors are acceptable (below 14 %), all QC approaches fail to identify in which bond the largest history variable occurs. This can be verified in Fig. 17a, where the bonds with the extreme plastic slips are presented by thick lines for the different systems. Note that the presented results correspond to the central summation rule only.

6. Summary and Conclusions

An analysis of the QuasiContinuum (QC) approach for regular lattice systems with internal dissipative processes is presented based on the variational, energy-consistent formulation of Mielke and Roubíček (2015). The main results can be summarized as follows:

1. The virtual-power-based QC method introduced by Beex et al. (2014c) can be equivalently derived from an appropriate energy potential. As both QC schemes satisfy the energy balance, the variational structure of the virtual-power-based QC method is confirmed by this study.
2. As a consequence of the central summation rule, the number of internal variables is highly reduced. An alternative approach may be to introduce geometrical constraints for the internal variables, possibly allowing a unique reconstruction of all unknowns (instead of only the kinematic variables). We have outlined briefly this perspective and emphasized the differences from the summation rule assumption.
3. In the section describing the solution strategies, an alternating minimization method for nonsmooth potentials was specified for the QC framework.
4. The example section has demonstrated the energy consistency of different QC schemes for three benchmark examples involving uniform loading, pure bending, and indentation test. In spite of large computational savings, all approximate solutions for all examples proved to be in a good agreement with the full-lattice solution in terms of stored and dissipated energies (by accepting errors in energies only up to 4 %, the number of degrees of freedom may be reduced up to the factor of 50).

The presented variational QC framework generalizes the original energy-based conservative quasicontinuum methodology for an entire class of rate-independent interactions and can easily be adjusted to incorporate e.g. damage phenomena merely by appropriate modifications of the energies. In addition, our results provide a convenient framework for adaptive variational QC methods in regular lattice networks with dissipative interactions, with potential applications in, e.g., fracture simulations of woven fabrics or polymers. All these topics are, nevertheless, beyond the scope of this contribution and will be reported separately.

Appendix A. Explicit Forms of Gradients and Hessians

For the sake of completeness, we provide in this appendix the derivatives of Π^k_{red}, recall Eq. (25), with respect to $\widehat{\boldsymbol{r}}$ explicitly. The internal force associated with atom α, $\boldsymbol{f}^\alpha_{\mathrm{int}} \in \mathbb{R}^{2\,n_{\mathrm{ato}}}$, reads as

$$\begin{aligned}\boldsymbol{f}^\alpha_{\mathrm{int}}(\widehat{\boldsymbol{r}}) = \frac{\partial \widehat{\pi}^k_{\mathrm{red},\alpha}(\widehat{\boldsymbol{r}}, \widehat{\boldsymbol{z}}_{\mathrm{p}}; \boldsymbol{q}(t_{k-1}))}{\partial \widehat{\boldsymbol{r}}} = \frac{1}{2}\sum_{\beta\in B_\alpha} \frac{\partial \phi^{\alpha\beta}(\widehat{r}^{\alpha\beta}, \widehat{z}^{\alpha\beta}_{\mathrm{p}})}{\partial \widehat{\boldsymbol{r}}^\gamma} = \\ = \frac{1}{2}\sum_{\beta\in B_\alpha} \phi' \frac{\widehat{\boldsymbol{r}}^{\alpha\beta}}{\widehat{r}^{\alpha\beta}}(\delta^{\beta\gamma} - \delta^{\alpha\gamma}),\ \gamma = 1,\dots,n_{\mathrm{ato}},\end{aligned} \tag{A.1}$$

where $\widehat{\pi}^k_{\mathrm{red},\alpha}$ denotes the reduced incremental site energy of atom α with condensed variable $\widehat{\boldsymbol{z}}_{\mathrm{c}}$, see also Eqs. (14b) and (25). The global force is then expressed as

$$\boldsymbol{f}(\widehat{\boldsymbol{r}}) = \sum_{\alpha=1}^{n_{\mathrm{ato}}} \boldsymbol{f}^\alpha_{\mathrm{int}}(\widehat{\boldsymbol{r}}). \tag{A.2}$$

Note that if external force vector $\boldsymbol{f}_{\mathrm{ext}}$ is present, it is simply subtracted from the right-hand-side of Eq. (A.2). The stiffness matrix associated with an atom site α, $\boldsymbol{K}^\alpha \in \mathbb{R}^{2\,n_{\mathrm{ato}}} \times \mathbb{R}^{2\,n_{\mathrm{ato}}}$, reads as

$$\begin{aligned}\boldsymbol{K}^\alpha(\widehat{\boldsymbol{r}}) = \frac{\partial^2 \widehat{\pi}^k_{\mathrm{red},\alpha}(\widehat{\boldsymbol{r}}, \widehat{\boldsymbol{z}}_{\mathrm{p}}; \boldsymbol{q}(t_{k-1}))}{\partial \widehat{\boldsymbol{r}} \partial \widehat{\boldsymbol{r}}} = \frac{1}{2}\sum_{\beta\in B_\alpha} \frac{\partial^2 \phi^{\alpha\beta}(\widehat{r}^{\alpha\beta}, \widehat{z}^{\alpha\beta}_{\mathrm{p}})}{\partial \widehat{\boldsymbol{r}}^\gamma \partial \widehat{\boldsymbol{r}}^\delta} = \\ = \frac{1}{2}\sum_{\beta\in B_\alpha} \left[\frac{\phi'}{\widehat{r}^{\alpha\beta}}\delta_{mn} + \left(\frac{\phi''}{(\widehat{r}^{\alpha\beta})^2} - \frac{\phi'}{(\widehat{r}^{\alpha\beta})^3}\right)\widehat{\boldsymbol{r}}^{\alpha\beta}\otimes\widehat{\boldsymbol{r}}^{\alpha\beta}\right](\delta^{\beta\gamma} - \delta^{\alpha\gamma})(\delta^{\beta\delta} - \delta^{\alpha\delta}), \\ m,n = 1,2,\ \gamma,\delta = 1,\dots,n_{\mathrm{ato}},\end{aligned} \tag{A.3}$$

whereas global stiffness is expressed as

$$\boldsymbol{K}(\widehat{\boldsymbol{r}}) = \sum_{\alpha=1}^{n_{\mathrm{ato}}} \boldsymbol{K}^\alpha(\widehat{\boldsymbol{r}}). \tag{A.4}$$

Here, we have used the relation

$$\frac{\partial \widehat{r}^{\alpha\beta}}{\partial \widehat{r}^\gamma_m} = \frac{\widehat{r}^{\alpha\beta}_m}{\widehat{r}^{\alpha\beta}}(\delta^{\beta\gamma} - \delta^{\alpha\gamma}),\ m = 1,2, \tag{A.5}$$

and for brevity we have denoted

$$\phi' = \frac{\partial \phi^{\alpha\beta}(\widehat{r}^{\alpha\beta}, \widehat{z}_{\mathrm{p}}^{\alpha\beta})}{\partial \widehat{r}^{\alpha\beta}}, \quad \phi'' = \frac{\partial^2 \phi^{\alpha\beta}(\widehat{r}^{\alpha\beta}, \widehat{z}_{\mathrm{p}}^{\alpha\beta})}{\partial (\widehat{r}^{\alpha\beta})^2}. \tag{A.6}$$

Above, m, n relate to spatial dimensions, α, β relate to atoms, δ_{mn} denotes the Kronecker-delta product with respect to spatial coordinates, $\delta^{\alpha\beta}$ denotes the Kronecker-delta product with respect to atoms, and $\boldsymbol{a} \otimes \boldsymbol{b} = a_m b_n$ denotes the tensor product of vectors $\boldsymbol{a}$ and $\boldsymbol{b}$.

Acknowledgements

Financial support for this work from the Czech Science Foundation (GAČR) under project No. 14-00420S is gratefully acknowledged.

Amelang, J.S., Venturini, G.N., Kochmann, D.M., 2015. Summation rules for a fully nonlocal energy-based quasicontinuum method. Journal of the Mechanics and Physics of Solids 82, 378–413. URL: http://www.sciencedirect.com/science/article/pii/S0022509615000630, doi: http://dx.doi.org/10.1016/j.jmps.2015.03.007.

Beex, L.A.A., Kerfriden, P., Rabczuk, T., Bordas, S.P.A., 2014a. Quasicontinuum-based multiscale approaches for plate-like beam lattices experiencing in-plane and out-of-plane deformation. Computer Methods in Applied Mechanics and Engineering 279, 348–378. URL: http://www.sciencedirect.com/science/article/pii/S0045782514002047, doi: http://dx.doi.org/10.1016/j.cma.2014.06.018.

Beex, L.A.A., Peerlings, R.H.J., Geers, M.G.D., 2011. A quasicontinuum methodology for multiscale analyses of discrete microstructural models. International Journal for Numerical Methods in Engineering 87, 701–718. URL: http://dx.doi.org/10.1002/nme.3134, doi: 10.1002/nme.3134.

Beex, L.A.A., Peerlings, R.H.J., Geers, M.G.D., 2014b. Central summation in the quasicontinuum method. Journal of the Mechanics and Physics of Solids 70, 242–261. URL: http://www.sciencedirect.com/science/article/pii/S0022509614001100, doi: http://dx.doi.org/10.1016/j.jmps.2014.05.019.

Beex, L.A.A., Peerlings, R.H.J., Geers, M.G.D., 2014c. A multiscale quasicontinuum method for dissipative lattice models and discrete networks. Journal of the Mechanics and Physics of Solids 64, 154–169. URL: http://www.sciencedirect.com/science/article/pii/S0022509613002445, doi: http://dx.doi.org/10.1016/j.jmps.2013.11.010.

Beex, L.A.A., Peerlings, R.H.J., Geers, M.G.D., 2014d. A multiscale quasicontinuum method for lattice models with bond failure and fiber sliding. Computer Methods in Applied Mechanics and Engineering 269, 108–122. URL: http://www.sciencedirect.com/science/article/pii/S004578251300279X, doi: http://dx.doi.org/10.1016/j.cma.2013.10.027.

Beex, L.A.A., Peerlings, R.H.J., van Os, K., Geers, M.G.D., 2015a. The mechanical reliability of an electronic textile investigated using the virtual-power-based quasicontinuum method. Mechanics of Materials 80, Part A, 52–66. URL: http://www.sciencedirect.com/science/article/pii/S0167663614001495, doi: http://dx.doi.org/10.1016/j.mechmat.2014.08.001.

Beex, L.A.A., Rokoš, O., Zeman, J., Bordas, S.P.A., 2015b. Higher-order quasicontinuum methods for elastic and dissipative lattice models: uniaxial deformation and pure bending. GAMM-Mitteilungen 38, 344–368. URL: http://dx.doi.org/10.1002/gamm.201510018, doi: 10.1002/gamm.201510018.

Bonnans, J.F., Gilbert, J.C., Lemaréchal, C., Sagastizábal, C.A., 2006. Numerical Optimization: Theoretical and Practical Aspects (Universitext). Springer-Verlag New York, Inc., Secaucus, NJ, USA. doi: 10.1007/978-3-540-35447-5.

Bourdin, B., Francfort, G.A., Marigo, J.J., 2000. Numerical experiments in revisited brittle fracture. Journal of the Mechanics and Physics of Solids 48, 797–826. URL: http://www.sciencedirect.com/science/article/pii/S0022509699000289, doi: http://dx.doi.org/10.1016/S0022-5096(99)00028-9.

Byrne, C., 2013. Alternating minimization as sequential unconstrained minimization: A survey. Journal of Optimization Theory and Applications 156, 554–566. URL: http://dx.doi.org/10.1007/s10957-012-0134-2, doi: 10.1007/s10957-012-0134-2.

Carstensen, C., Hackl, K., Mielke, A., 2002. Non-convex potentials and microstructures in finite-strain plasticity. R. Soc. Lond. Proc. Ser. A Math. Phys. Eng. Sci. 458, 299–317. doi: 10.1098/rspa.2001.0864.

Charlotte, M., Francfort, G., Marigo, J.J., Truskinovsky, L., 2000. Revisiting brittle fracture as an energy minimization problem: Comparisons of Griffith and Barenblatt surface energy models, in: Symposium on Continuous Damage and Fracture. URL: http://www.gillesfrancfort.com/Site/Publications_files/published.version.CFMT00%20copy.pdf.

Chen, J., García-Cervera, C.J., Li, X., 2015. An atomistic/continuum coupling method using enriched bases. Multiscale Modeling & Simulation 13, 766–789. URL: http://epubs.siam.org/doi/abs/10.1137/140990644, doi: 10.1137/140990644.

Conti, S., Ortiz, M., 2008. Minimum principles for the trajectories of systems governed by rate problems. Journal of the Mechanics and Physics of Solids 56, 1885–1904. URL: http://www.sciencedirect.com/science/article/pii/S0022509607002220, doi: http://dx.doi.org/10.1016/j.jmps.2007.11.006.

Csiszár, I., Tusnády, G., 1984. Information geometry and alternating minimization procedures. Statistics and Decisions 1, 205–237.

Curtin, W.A., Miller, R.E., 2003. Atomistic/continuum coupling in computational materials science. Modelling and Simulation in Materials Science and Engineering 11, R33. URL: http://stacks.iop.org/0965-0393/11/i=3/a=201, doi: 10.1088/0965-0393/11/3/201.

Francfort, G.A., Marigo, J.J., 1993. Stable damage evolution in a brittle continuous medium. European Journal of Mechanics-A/Solids 12, 149–149.

Francfort, G.A., Marigo, J.J., 1998. Revisiting brittle fracture as an energy minimization problem. Journal of the Mechanics and Physics of Solids 46, 1319–1342. URL: http://www.sciencedirect.com/science/article/pii/S0022509698000349, doi: http://dx.doi.org/10.1016/S0022-5096(98)00034-9.

Fritzen, F., Hodapp, M., Leuschner, M., 2014. GPU accelerated computational homogenization based on a variational approach in a reduced basis framework. Computer Methods in Applied Mechanics and Engineering 278, 186–217. URL: http://www.sciencedirect.com/science/article/pii/S0045782514001510, doi: http://dx.doi.org/10.1016/j.cma.2014.05.006.

Hackl, K., Fischer, F.D., 2008. On the relation between the principle of maximum dissipation and inelastic evolution given by dissipation potentials. Proceedings of the Royal Society of London A: Mathematical, Physical and Engineering Sciences 464, 117–132. URL: http://rspa.royalsocietypublishing.org/content/464/2089/117, doi: 10.1098/rspa.2007.0086, arXiv:http://rspa.royalsocietypublishing.org/content/464/2089/117.full.pdf.

Han, W., Reddy, B.D., 1995. Computational plasticity: The variational basis and numerical analysis. Computational Mechanics Advances 2, 283–400.

Iyer, M., Gavini, V., 2011. A field theoretical approach to the quasi-continuum method. Journal of the Mechanics and Physics of Solids 59, 1506–1535. URL: http://www.sciencedirect.com/science/article/pii/S0022509610002425, doi: http://dx.doi.org/10.1016/j.jmps.2010.12.002.

Kochmann, D.M., Hackl, K., 2010. The evolution of laminates in finite crystal plasticity: a variational approach. Continuum Mechanics and Thermodynamics 23, 63–85. URL: http://dx.doi.org/10.1007/s00161-010-0174-5, doi: 10.1007/s00161-010-0174-5.

Kulachenko, A., Uesaka, T., 2012. Direct simulations of fiber network deformation and failure. Mechanics of Materials 51, 1–14. URL: http://www.sciencedirect.com/science/article/pii/S0167663612000683, doi: http://dx.doi.org/10.1016/j.mechmat.2012.03.010.

Kwon, S., Lee, Y., Park, J.Y., Sohn, D., Lim, J.H., Im, S., 2009. An efficient three-dimensional adaptive quasicontinuum method using variable-node elements. Journal of Computational Physics 228, 4789–4810. URL: http://www.sciencedirect.com/

science/article/pii/S002199910900165X, doi: http://dx.doi.org/10.1016/j.jcp.2009.03.028.

Liu, J.X., Chen, Z.T., Li, K.C., 2010. A 2-d lattice model for simulating the failure of paper. Theoretical and Applied Fracture Mechanics 54, 1–10. URL: http://www.sciencedirect.com/science/article/pii/S016784421000039X, doi: http://dx.doi.org/10.1016/j.tafmec.2010.06.009.

Luskin, M., Ortner, C., 2013. Atomistic-to-continuum coupling. Acta Numerica 22, 397–508. URL: http://journals.cambridge.org/article_S0962492913000068, doi: 10.1017/S0962492913000068.

Mielke, A., 2002. Geometry, Mechanics, and Dynamics. Springer New York, New York, NY. chapter Finite Elastoplasticity Lie Groups and Geodesics on SL(d). pp. 61–90. URL: http://dx.doi.org/10.1007/0-387-21791-6_2, doi: 10.1007/0-387-21791-6_2.

Mielke, A., 2004. Deriving new evolution equations for microstructures via relaxation of variational incremental problems. Computer Methods in Applied Mechanics and Engineering 193, 5095–5127. URL: http://www.sciencedirect.com/science/article/pii/S0045782504002683, doi: http://dx.doi.org/10.1016/j.cma.2004.07.003. advances in Computational Plasticity.

Mielke, A., Roubíček, T., 2015. Rate-Independent Systems: Theory and Application. 1 ed., Springer-Verlag New York. URL: http://www.springer.com/us/book/9781493927050, doi: 10.1007/978-1-4939-2706-7.

Mielke, A., Theil, F., 2004. On rate-independent hysteresis models. Nonlinear Differential Equations and Applications NoDEA 11, 151–189. URL: http://dx.doi.org/10.1007/s00030-003-1052-7, doi: 10.1007/s00030-003-1052-7.

Miller, R., Tadmor, E., 2009. A unified framework and performance benchmark of fourteen multiscale atomistic/continuum coupling methods. Modelling and Simulation in Materials Science and Engineering 17. URL: http://stacks.iop.org/0965-0393/17/i=5/a=053001, doi: 10.1088/0965-0393/17/5/053001.

Miller, R.E., Tadmor, E.B., 2002. The quasicontinuum method: Overview, applications and current directions. Journal of Computer-Aided Materials Design 9, 203–239. URL: http://dx.doi.org/10.1023/A%3A1026098010127, doi: 10.1023/A:1026098010127.

Ortiz, M., Repetto, E.A., 1999. Nonconvex energy minimization and dislocation structures in ductile single crystals. Journal of the Mechanics and Physics of Solids 47, 397–462. URL: http://www.sciencedirect.com/science/article/pii/S0022509697000963, doi: http://dx.doi.org/10.1016/S0022-5096(97)00096-3.

Ortiz, M., Stainier, L., 1999. The variational formulation of viscoplastic constitutive updates. Computer Methods in Applied Mechanics and Engineering 171, 419–444. URL: http://

www.sciencedirect.com/science/article/pii/S0045782598002199, doi: http://dx.doi.org/10.1016/S0045-7825(98)00219-9.

Pham, K., Marigo, J.J., 2013. From the onset of damage to rupture: construction of responses with damage localization for a general class of gradient damage models. Continuum Mechanics and Thermodynamics 25, 147–171. URL: http://dx.doi.org/10.1007/s00161-011-0228-3, doi: 10.1007/s00161-011-0228-3.

Pham, K., Marigo, J.J., Maurini, C., 2011. The issues of the uniqueness and the stability of the homogeneous response in uniaxial tests with gradient damage models. Journal of the Mechanics and Physics of Solids 59, 1163–1190. URL: http://www.sciencedirect.com/science/article/pii/S002250961100055X, doi: http://dx.doi.org/10.1016/j.jmps.2011.03.010.

Potluri, P., Manan, A., 2007. Mechanics of non-orthogonally interlaced textile composites. Composites Part A: Applied Science and Manufacturing 38, 1216–1226. URL: http://www.sciencedirect.com/science/article/pii/S1359835X06001813, doi: http://dx.doi.org/10.1016/j.compositesa.2006.04.008.

Quarteroni, A., Gianluigi, R. (Eds.), 2014. Reduced Order Methods for Modeling and Computational Reduction. Springer International Publishing. doi: 10.1007/978-3-319-02090-7.

Radovitzky, R., Ortiz, M., 1999. Error estimation and adaptive meshing in strongly nonlinear dynamic problems. Computer Methods in Applied Mechanics and Engineering 172, 203 – 240. URL: http://www.sciencedirect.com/science/article/pii/S0045782598002308, doi: http://dx.doi.org/10.1016/S0045-7825(98)00230-8.

Rokoš, O., Zeman, J., Jirásek, M., 2016. Localization analysis of an energy-based fourth-order gradient plasticity model. European Journal of Mechanics-A/Solids 55, 256–277. URL: http://www.sciencedirect.com/science/article/pii/S099775381500128X, doi: http://dx.doi.org/10.1016/j.euromechsol.2015.09.007.

Roubíček, T., 2005. Nonlinear Partial Differential Equations with Applications. International Series of Numerical Mathematics, Birkhaüser-Verlag. URL: http://www.springer.com/us/book/9783034805124?token=prtst0416p, doi: 10.1007/978-3-0348-0513-1.

Schröder, J., Hackl, K., 2013. Plasticity and Beyond: Microstructures, Crystal-Plasticity and Phase Transitions. Springer Publishing Company, Incorporated. URL: http://www.springer.com/us/book/9783709116241, doi: 10.1007/978-3-7091-1625-8.

Simo, J.C., Hughes, T.J.R., 2000. Computational Inelasticity. Interdisciplinary Applied Mathematics, Springer New York. URL: http://www.springer.com/gp/book/9780387975207?token=prtst0416p, doi: 10.1007/b98904.

Tadmor, E.B., Miller, R.E., 2011. Modeling Materials: Continuum, Atomistic and Multiscale Techniques. Cambridge University Press. URL: http://www.cambridge.org/cz/academic/subjects/physics/computational-science-and-modelling/modeling-materials-continuum-atomistic-and-multiscale-techniques.

Tadmor, E.B., Ortiz, M., Phillips, R., 1996. Quasicontinuum analysis of defects in solids. Philosophical Magazine A 73, 1529–1563. URL: http://dx.doi.org/10.1080/01418619608243000, doi: 10.1080/01418619608243000.

Xiao, S., Yang, W., 2007. A temperature-related homogenization technique and its implementation in the meshfree particle method for nanoscale simulations. International Journal for Numerical Methods in Engineering 69, 2099–2125. URL: http://dx.doi.org/10.1002/nme.1841, doi: 10.1002/nme.1841.

Yang, Q., To, A.C., 2015. Multiresolution molecular mechanics: A unified and consistent framework for general finite element shape functions. Computer Methods in Applied Mechanics and Engineering 283, 384–418. URL: http://www.sciencedirect.com/science/article/pii/S0045782514003545, doi: http://dx.doi.org/10.1016/j.cma.2014.09.031.